TECHNISCHE UNIVERSITÄT WIEN
Vienna University of Technology

D I P L O M A R B E I T

Der Einfluss von Kollimatorlamellensequenzierung und Fehler in der Dosimetrie kleiner Felder auf die dosimetrische Genauigkeit von Behandlungsplänen in der Strahlentherapie

Ausgeführt am Atominstitut

der Technischen Universität Wien

Unter der Anleitung von Univ. Prof. Dipl. Ing. Dr. Dietmar Georg and Dipl. Ing. Wolfgang Lechner, PhD

durch
Alexander Primeßnig BSc

Handelskai 390/12/10
1020 Wien

August 21, 2016

'Though thy crest be shorn and shaven, thou,' I said, 'art sure no craven,
Ghastly grim and ancient Raven wandering from the Nightly shore -
Tell me what thy lordly name is on the Night's Plutonian shore!'

The Raven, E. A. Poe

Declaration

I, Alexander Primeßnig BSc, declare that this thesis submitted in partial fulfilment of the requirements for the conferral of the degree Master of Science, from the University of Technology, Vienna, is wholly my own work unless otherwise referenced or acknowledged. This document has not been submitted for qualifications at any other academic institution.

Alexander Primeßnig BSc
August 21, 2016

Abstract

In this work, the influence of errors in the dosimetry of small fields on dosimetric treatment plan quality was investigated for four different anatomical sites. Brain metastases, prostate including lymph nodes, prostate boost and head & neck were considered in the study. The measured dose distributions of the treatment plans were compared with calculated dose distributions generated by iPlan (Brainlab AG, Feldkirchen, Germany) (IMRT) and Monaco (Elekta, Stockholm, Sweden)(VMAT) using a gamma pass rate analysis (GPR). The calculated dose distributions were based on a clinical used beam model (BM) and a beam model with erroneous output factors (OF), designed to account for the influence of uncertainties in small field dosimetry. The measurements were made using radiochromic films. Additionally a three-dimensional GPR-analysis comparing the calculated doses of both beam models using 3D Slicer, a widely used software tool in radiation therapy (RT) was conducted. In order to map small field dosimetry errors and the resulting GPR to the specific geometry of a treatment plan, DICOM data containing treatment plan specifications were analyzed and the aperture distribution for each plan was calculated. Out of this, a model based on the difference in OFs between the clinical BM and the modified BM was designed and implemented into Matlab. Correlations were analyzed between the error factors generated by this model and the GPR result based on the clinically used beam model. Furthermore, a correlation analysis of the GPR based on comparison of measurement with clinical BM and modified BM was conducted. The overall GPR using a criterion of 3 %/3 mm, conducted with 3D Slicer, was well above 95 %. The GPRs based on comparisons of calculated and measured dose of both BMs using the same criterion, was mostly > 90 %, except 5 outliers out of 46 considered treatment plans. There was no correlation found for any treatment

group evaluated between the error factors generated by the above mentioned model and the GPR results based on the clinical BM. However, there was a significant correlation found for 2 treatment groups between the GPR based on the modified BM and the clinical BM, both showing better results for the modified BM. Finally, the general dependencies and restrictions are presented and an additional error model based on Clarkson integration is outlined. In this work it was found, that small field errors did not translate into unacceptable GPR. It was also found, that the BM modification lead to sensitive areas in the region of steep dose gradients, but so far a reason for this could not be investigated. Furthermore, the assessment of error factors is not trivial and the proposed model to generate error factors for an arbitrary leaf constellation probably needs further improvement. The concept of GPR-analysis was also discussed in detail and it was concluded, that the method has its difficulties in terms of comparability.

Acknowledgments

I would like to kindly and sincerely thank Univ.-Prof. Dipl.-Ing. Dr. Dietmar Georg, who gave me the chance to write my diploma thesis in the fascinating area of radiation physics and radiation therapy. Indeed, I learned a lot, scientifically as well as in clinical practice, which was of outmost interest to me and definitely enhanced my wealth of experience.

Secondly, I would like to thank my direct supervisor Wolfgang Lechner, PhD, whose patience and time I demanded quite often and despite the stressful clinical working processes, he always took time to answer my questions. I do appreciate that.

I would also like to thank everybody working in the Division of Medical Radiation Physics, Department of Radiation Oncology or linked departments for answering my questions and helping me to orientate in this multidisciplinary field.

I thank my family and friends. I cannot imagine successfully studying physics without their great support and help. Finally, I would like to express special thanks to my girlfriend, relentlessly supporting me with truthfully invaluable advice and assurance.

List of Abbrevations

AKH	Allgemeins Krankenhaus
BM	Beam Model
CT	Computer Tomography
DD	Dose Deviation
DICOM	Digital Imaging and Communications in Medicine
DTA	Distance To Agreement
FF	Flattening Filter
FFF	Flattening Filter Free
GPR	Gamma Pass Rate
HN	Head and Neck
IAEA	International Atomic Energy Agency
IGRT	Image Guided Radiation Therapy
IMRT	Intensity Modulated Radiation Therapy
LINAC	Linear Accelerator
MC	Monte Carlo
MLC	Multileaf Collimator
MU	Monitor Units
MUV	Medical University Vienna
OAR	Organs at Risk
OD	Optical Density
OF	Output Factor
PB	Pencil Beam
PTV	Planning Target Volume
QA	Quality Assurance
ROI	Region of Interest
RT	Radiation Therapy

sas	step and shoot
SBRT	Stereotactic Body Radiation Therapy
SRT	Stereotactic Radiation Therapy
SSD	Source to Surface Distance
TPS	Treatment Planning System
VMAT	Volumetric Modulated Arc Therapy

Contents

Chapter 1

Introduction and theoretical background

In 2012, an estimated number of 14.1 million new cancer cases occurred around the world [1], which makes this disease one of the biggest health issues of mankind. In Austria, approximately 39000 new incidents of malignant tumors have been diagnosed in 2012 out of which a cancer risk of nearly 30% can be calculated. [25] In other words, statistically one out of three will at one point in his or her life suffer from this disease.

Because of the large numbers of incidences and the very treacherous character of this disease, enormous effort has been put into research in recent years to find proper treatment methods, to improve existing ones and to understand its complicated mechanisms. The actual difficulty in treating cancer lies in the similarity to normal tissue. This is also the reason why treatment methods often have considerably negative side effects: Most treatment methods also damage healthy tissue, as tumor cells can barely be distinguished from normal cells. [20]

Basically, cancer therapy is based on three pillars: surgical intervention, chemotherapy and radiation therapy (RT). Usually, two or more techniques are combined during the entire treatment procedure. [26] Sometimes also targeted therapy or immune therapy is used. [26] Malignant tumor cells have shown to be more sensitive to ionizing radiation, than normal tissue. [27,29] Exploiting this fact, makes the therapeutic effect of radiation therapy possible. An graphical outline of the

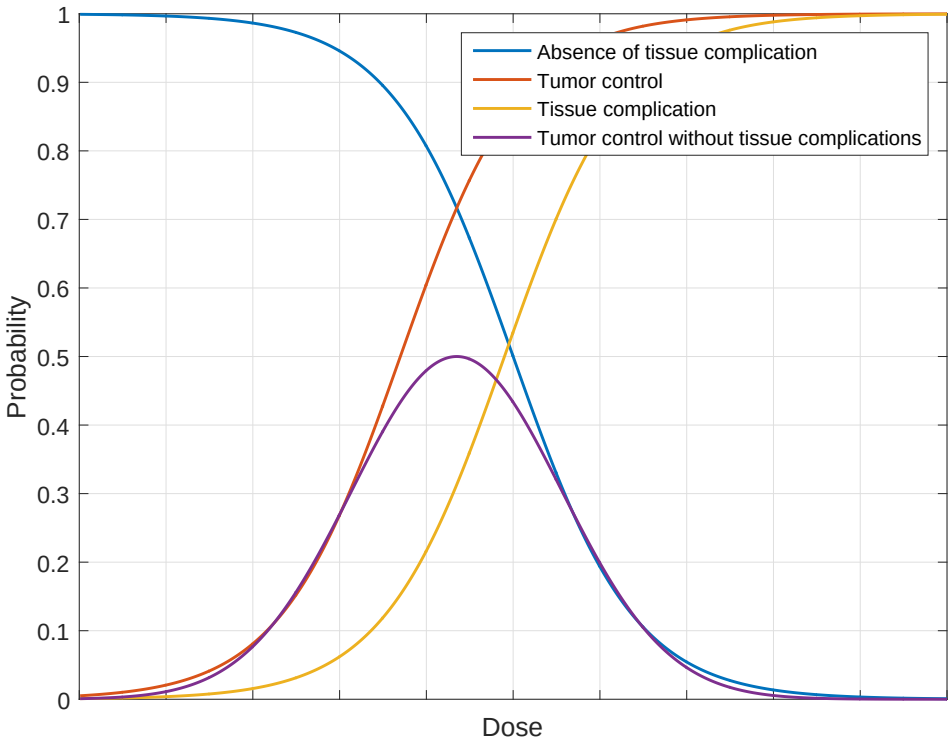

Figure 1.1: The therapeutic window in radiation therapy is shown. The area below the purple curve is the worthwhile region for a treatment. The template of this figure was obtained from literature.[69]

resulting therapeutic window is shown in figure 1.1. This graph shows, that it is always a balancing act between ablating the tumor and sparing tissue.

Within clinical RT, brachytherapy and teletherapy can be differentiated by the way a certain amount of dose is delivered to the human body. Patients treated with the brachytherapeutical approach directly get in contact with sealed radioactive sources. It can be implanted for a longer period of time (Seeds) or just put on the malignant growth for a short duration and removed afterwards (afterloading).[20] The teletherapeutical approach uses radiation delivered to the human body from a greater distance. In clinical treatment procedures linear accelerators (linacs) are often used. However, also ion therapy facilities, mostly using protons or carbon ions for treatment were built. These particles generally have a different interaction behaviour in terms of dose distribution in human tissue compared to photons. One of their typical properties in this context is the Bragg peak, which represents a maximum of dose deposition in tissue. After this peak, there is a steep dose falloff, which is of high practical

importance for radiation therapy, as tissue after this peak can be spared.

In the last decades radiation therapy evolved rapidly resulting in a highly complex and interdisciplinary field in which physicians, physicists, biologists and engineers are required to work closely together not only to maintain the clinical workflow, but also to further focus on research to improve treatment techniques of malignant growths.

1.1 Aspects of radiation therapy

If a tumour is detected, for instance on a patient's scan obtained from medical imaging systems such as computer tomography (CT), positron emission tomography (PET) or magnetic resonance tomography (MRT) and radiation therapy is decided to be one of the treatment methods, the physician delineates the visible malignant growth and the organs at risk (OAR) using a suitable treatment planning system (TPS). The actual tumor visible, commonly referred to as gross target volume (GTV) with additional margins accounting for microscopical outgrowths makes up the cross target volume (CTV). If additional margins for the organ motion and the radiation therapy setup itself are applied, the volume is called planning target volume (PTV). Using the latter volume is considered when planning a treatment with a TPS [20]. Generally, every treatment planning procedure requires an accurate dose calculation.

As far as treatment planning is concerned, there are different methods of dose delivery in the human body.

Prior to the development of rather complex treatment procedures such as intensity modulated radiation therapy (IMRT) and volumetric arc therapy (VMAT), single fields or beams were widely used. The introduction of a dynamically adjustable and flexible MLC in the mid 90s of the previous century, made more complex treatment methods possible. Before this technique was commercialized, the geometry of a field was shaped by manually mounting fixed collimators below the linac aperture, which also led to an extended time effort. [20]

Conformal fields are used as well as step and shoot (sas), dynamic IMRT and VMAT. The difference mostly lies in timing of gantry motion and leaf sequenc-

ing: When delivering conformal treatment plans, the fields and therewith the MLC does not change within a beam. However, when using IMRT the gantry angles are fixed while the leaves of the multi leaf collimator (MLC) are moving discretely (sas IMRT) or continouisly (dynamic IMRT). In contrast, when treating with VMAT, the gantry and the MLC moves continuously. The latter generally produces larger areas of low dose in the patient but the treatment duration is shorter. [20,27]

Treatment plans are usually delivered in 2 Gy fractions. Treatment techniques which make use of a higher dose per fraction are referred to as stereotactic radiation therapy (SRT) for cranial growths and stereotactic body radiation therapy (SBRT) for tumors in extracranial areas. These methods are among other purposes used for the palliative treatment of metastases. The high delivered dose and therewith a higher biological dose simply has the advantage of faster ablating the malignant growth. However, because of the high dose, this treatment technique makes an accurate patient positioning even more vital. If the high dose is delivered in one single fraction, this treatment method is referred to as stereotactic radiation surgery (SRS) or stereotactic body radiation surgery (SRBS), respectively. [20]

The planning procedure focuses on putting the prescribed dose to the PTV while sparing normal tissue and especially OAR at the same time. The planning of conformal treatment plans is commonly referred to as forward planing. This means, that the beams are planned manually and optimization is based on the expert's experience. On the contrary IMRT and VMAT are based on inverse planning, meaning that the problem of delivering dose to the tumor while sparing OAR is solved by suitable programs. The TPS use algorithms to compute the planned dose, of which Monte Carlo (MC) and Pencil Beam (PB) algorithms are of importance. A brief introduction of these algorithms is given in chapter 1.4. [5,20]

1.1.1 Physical interactions

As this work deals with photon radiation, the basic physical relations and properties of photons interacting with materials shall be briefly explained.

If a photon moves towards matter, a number of interaction processes can occur:

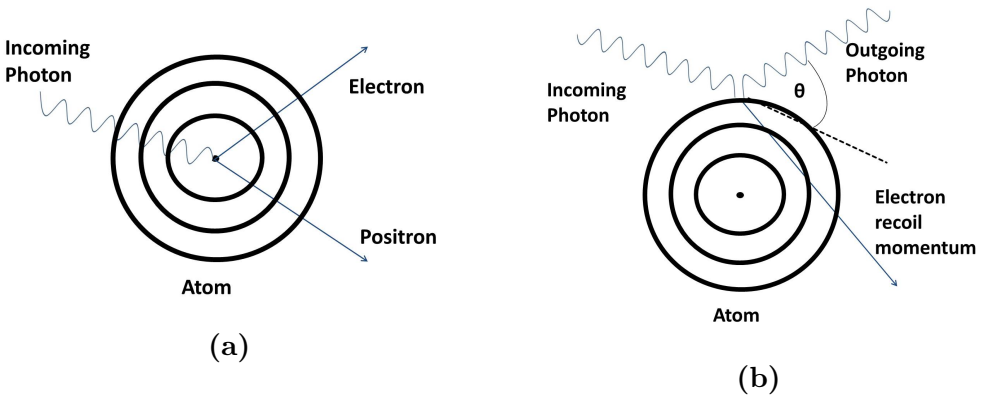

Figure 1.2: Illustrations of the two main interaction processes of photons in radiation therapy: pair production (a) and Compton scattering (b).

photoeffect, compton scattering, pair production, coherent scattering, triplet production and the nuclear photoeffect. These effects can be summarized in a (differential) cross section, denoted σ_{tot}

$$\sigma_{tot} = \sigma_{pair} + \sigma_{phot} + \sigma_{trip} + \sigma_{comp} + \sigma_{coh} + \sigma_{nphot} \tag{1.1}$$

The cross section has the dimensions of an area and its value gives the interaction probability of the particle. It is also the basis of every MC and PB code calculating dose distributions for a treatment plan.[20,5] At the energies used in radiation therapy (between 3 MV and 30 MV) pair production and Compton scattering are of main relevance[7], which are therefore, together with the photoelectric effect, described in greater detail.

Pair production

This effect denotes the production of electron-positron pairs in the electromagnetic field of the nucleus. A sketch of this mechanism is shown in figure 1.2a. Pair production is a typical high energy phenomenon, as the photon is required to have a minimum energy of $1022\,keV$. The reason for this lies in the rest masses of the produced constituents, as not only the electron, but also its antiparticle have rest energies of $511\,keV$. The positron is likely to annihilate with an electron in the atomic shell, leading to the production of a photon with minimum energy of $1022\,keV$.

Compton scattering

Compton scattering occurs if photons scatter inelastically, i.e. energy transfer occurs from photons to electrons in the atomic shell, as indicated in figure 1.2b. The change in wavelength of the photon can be calculated easily using the conservation of energy and momentum leading to

$$\lambda' - \lambda = \frac{h}{m_e c}(1 - \cos\theta), \tag{1.2}$$

in which λ is the wavelength of the incident photon, λ' the photon's wavelength after scattering, h the Planck constant, m_e the electron mass, c the speed of light and θ the scattering angle.

Up to an energy of about $25\,MeV$, the Compton effect is the dominating interaction process in water. Above this energy, the pair production is getting more dominant.

Photoelectric effect

This phenomenon, typically dominating in a lower energy range, represented a milestone in the evolving science of quantum mechanics about a hundred years ago. If a photon interacts, with an electron of an atomic shell, this electron can be removed from the atom i.e. the atom can be ionized. If ϕ is the work function of the electron, indicating the energy needed for leaving the atom and f denotes the frequency of the photon, the kinetic energy E_{kin} of the removed electron can be written as

$$E_{\text{kin}} = hf - \phi, \tag{1.3}$$

in which h is the Planck constant.

1.2 Medical linear accelerators and flattening filters

The primary purpose of a linac is the acceleration of charged particles by an frequently changing applied potential gradient. The general working principle of linacs is, that electrons are accelerated towards an anode [13] and during that

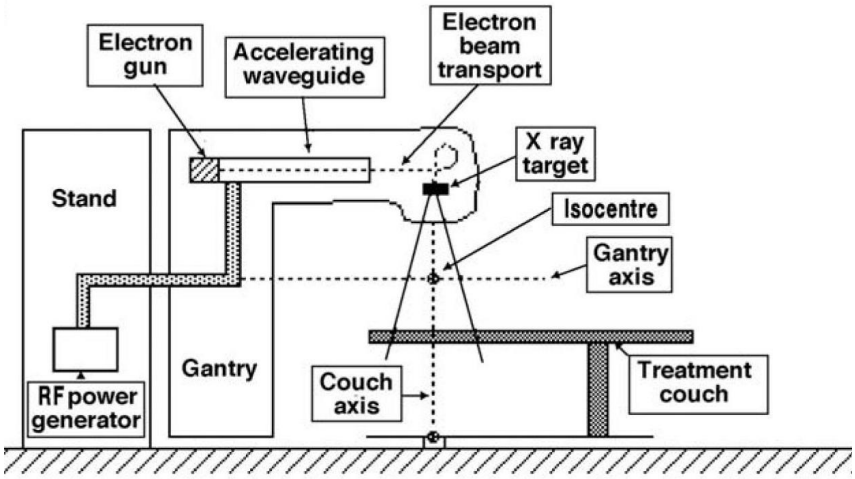

Figure 1.3: A sketch of a medical linac and its basic components is shown. The figure was extracted from lierature.[65]

process, focussed with bending magnets. A schematic sketch of a typical linear accelerator is shown in figure 1.3. Most linacs are capable of delivering photons and electrons, whereas the electron flow is achieved by replacing the target by a scatter foil.[41]

Flattening filter (FF) and flattening filter free (FFF) beams

A flattening filter (FF) is a several centimetre thick tool of conical shape in the treatment head designed to compensate the energy and intensity variation of the bremsstrahlung depending on the emission angle. This leads to a very flat dose profile only slightly disturbed by the central depression effect. These filters are being intensively used for decades. In the past, computational dose calculations were not available and a flat profile was desired, as dose estimation was eased. The rapid development of complex computer algorithms made research without flat dose profiles possible. Therefore, a number of research groups[13–15] are conducting clinical research without a FF to explore its properties and as a further goal, to integrate the advantages in clinical operation. A schematic comparison of FF and FFF operation is given in figure 1.4.

Flattening Filters are along with the primary and secondary collimator and the MLC the main source of scattering processes in the treatment head. One of the major effects when removing the FF is an about twofold increased dose rate[16]. This can be advantageous for SRT and SBRT, as for these techniques

a high dose is delivered at once. Therefore the treatment and the patient immobilization lasts less in FFF mode resulting in a higher patient comfort. Also FFF research on IMRT is conducted intensively [17], showing no difference between FF and FFF beams as far as treatment plan quality is concerned, but an increased number of MUs needed for FFF treatment plan delivery. Additionally, it has been shown, that the delivery times for IMRT and VMAT in FF and FFF mode are similar.

In addition to the increased dose rate, the well known phenomena of electron and neutron contamination can be decreased. It has been shown, that the former can mainly be contributed to the FF, especially at higher energies [18]. The neutron contamination was shown to be increasing absolutely, but decreasing relative to the photon flux.

As mentioned above, the FF also changes the spectrum. As the FF consists of materials with higher atomic numbers, the beam hardening effect affects the spectrum resulting in a less sharp bremsstrahlung peak in the spectrum compared to the FFF [13].

It was expected, that the dose calculation accuracy during treatment planing increases when removing the FF [13]. One reason for that is the often very simple modelling of electron contamination, which is reduced when removing the FF. Additionally, the spectrum dependence on distance from the central axis decreases without FF, which could lead to more accurate results. [58] However, it has been shown , that the FFF accuracy is not significantly improved compared to the FF beam. It was rather shown, that they are fairly equal. However, the dose calculation accuracy for off-axis profiles was observed to be higher for FFF beams than for FF. [23]

1.3 Small field dosimetry

It is also common and of interest in this work, to define a field size dependent factor representing the delivered dose at one point. The so called output factor (OF) is measured at a point on the central axis at a distance of 100 cm from the source. It is assumed, that this factor consists of two independent factors,

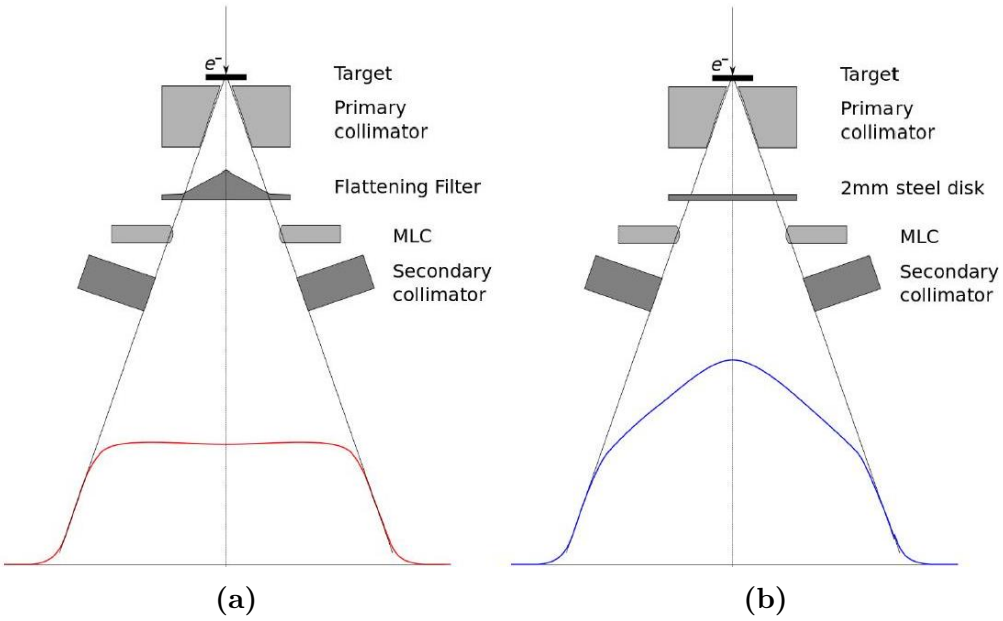

(a) **(b)**

Figure 1.4: Graphical representation of the treatment head in a linac in flattening filter (a) and flattening filter free (b) mode. The graph was extracted from literature [19]

the collimator scatter factor S_C and the phantom scatter factor S_P [20]

$$\mathrm{OF} = S_C \times S_P. \tag{1.4}$$

The development of SRT as well as advanced radiation techniques such as IMRT, motivated the research interest in dosimetry of small fields. The physical behaviour of fields sized lower than $4 \times 4\,\mathrm{mm}^2$ is different to that of larger fields as effects like electronic disequilibrium and source occlusion must be taken into account. [31–33] The charged particle equilibrium is important for the measurement accuracy, as it is a basic requirement for the validity of the Bragg-Gray cavity theory. When measuring the dose in small fields with a detector its chemical properties and the aspect of volume averaging, strongly correlated with the size of the detector must also be considered. [30]

In a volume in the center of a larger field, the amount and energy of secondary electrons scattered out equals roughly the number of electrons flowing in the volume. When considering a volume at the edge of a large field, or when dealing with very small fields, the field boundaries lead to a lower electron flux input compared to the electrons moving out. This is causing non equilibrium

conditions and is a potential source of errors.[33–32]

At a certain point, once the field size is too small, the source is not entirely viewable from the irradiated point of interest, which leads to a lower output, a blurred dose profile and an overestimated field size.[30]

The actual result when measuring small beams also depends on the detector's active volume. If the field size is small, the steep dose gradients making up the dose profile are also part of the measurement, which in further consequence leads to an averaged detector output not reflecting the dose at the particular point or area of interest. It is well known that for ion chambers, that the lack of electron equilibrium influences the measured output significantly more.[30]

For dosimetry measurements in radiation therapy

Besides ionization chambers a number of instruments such as diamond detectors, silicon diodes, alanine detectors etc. can be used for dosimetry measurements in radiation therapy. In order to estimate the impact of small fields a number of publications have been released comparing the output and behaviour of different detectors and providing correction factors for the effects described above[15,34–35]. Additionally, corrections in OFs and the corresponding error factors were stated, which represent the manifestation of the errors caused by small fields in TPS.[30–32,36–37] At fields down to $0.5 \times 0.5\,\mathrm{cm}^2$ OFs of about 0.5 have been reported[31] and detector specific correction factors of more than 10 %. The consequences of modifying these OFs in a beam model will also be investigated in this work.

1.4 Dose calculation

In order to work out a treatment plan for an intended treatment, a treatment planning system (TPS), a dose calculation software, is required to precisely map the dose distribution quantitatively. In this study, the TPS iPlan was used. There have been huge efforts made in the past 20 years, to develop adequate dose calculation algorithms. They are required to describe machine properties, ray propagation, material attenuation and interaction with its underlying physical effects. Two of these algorithms are presented here.

1.4.1 The Pencil Beam Algorithm

The beam is assumed to consist out of a large number of (theoretically) infinitesimal beamlets with infinitesimal cross section, propagating and undergoing interactions with a medium. The algorithm used by iPlan is entirely based on the publications of Mohan et. al.[2–4] Considering a small and monoenergetic pencil beam, the attenuation in a medium is exponential and the number of first collisions in a unit volume can therefore be written as[3,5]

$$N_{\mathrm{FC}}(E,d) = N_A e^{-\mu_{water}(E)d}\mu_{water}(E), \tag{1.5}$$

in which N_A represents the averaged number of photons with energy E and μ_{water} the linear attenuation coefficient in water of a depth d. Now the differential pencil beam (DPB) can be introduced as dose distribution per unit collision density relative to a point P of first collision $\mathrm{DPB}(|\vec{r}-\vec{r_Q}|,E)$. The DPB is usually generated by Monte Carlo (MC) simulations and is previously calculated and saved for different energies. It is not part of the PB calculation during a planning procedure. When integrating over all energies and over the depth in water the pencil beam dose can be calculated

$$D(\vec{r}) = \int\int N_{FC}(E,d)\, N_A e^{-\mu_{water}(E)d_P}\mu_{water}(E)\,\mathrm{DPB}(|\vec{r}-\vec{r_Q}|,E)\,\mathrm{d}E\mathrm{d}d_P. \tag{1.6}$$

This formula still describes the behaviour of just one pencil beam. If the entire idealized dose distribution (IDD) of the field is desired, the spatially depending photon fluence $\phi(\vec{r})$ must be taken into account, which can be accomplished by 2 dimensional convolution

$$\mathrm{IDD}(\vec{r}) = \int\int \phi(x',y',d)D(x'-x,y'-y,d)\mathrm{dx'dy'}. \tag{1.7}$$

Computationally, this integral is calculated with Fast Fourier Transformation (FFT). Finally, an arbitrary point in tissue can be computed to

$$D(\vec{r}) = \mathrm{IDD}(\vec{r})\,\mathrm{MU}\,\mathrm{NLOut}\,S_t(c_{mlc},c_{jaw})\,\mathrm{TPR}(l_{rad},c_d,\mathrm{coll})\left(\frac{\mathrm{SSD}_{cal}+d_{cal}}{\mathrm{SSD}+d}\right)^2 \tag{1.8}$$

with MU beeing the applied monitor units, IDD the idealized dose distribu-

tion, NLOut, the nominal linac output and TPR the tissue phantom ratio. Furthermore, $S_t(c_{\mathrm{mlc}}, c_{\mathrm{jaw}})$ represents the total scatter factor and describes the relative OF for a squared field. Finally, the source to surface distance used for measuring NLOut and the scatter factors SSD_{cal} is summed with the corresponding depth in tissue d_{cal} and divided by the values SSD and d of the actual measurement. [5]

1.4.2 The Monte Carlo Algorithm

In contrast to the previously explained PB algorithm, the MC algorithm generally simulates interaction such as scatter for each particle. The scattering cross sections in this case are represented by probability distributions and results are achieved by the use of statistical convergence. This leads to a potentially higher CPU effort, but also to a better result. The MC simulation in iPlan uses the XMVC algorithm based on publications of Fippel et. al.[7–8], which was initially designed for electron dose calculation[9]. This algorithm is about 15-20 times faster, than comparable MC algorithms such as EGS4[7,10]. The reason is a lower number of calculated photon histories and approximations justified by a characteristic parameter range of radiation therapy, such as the energy range. The idea behind the former, is to use one photon history more often, which is justified, if the considered photons are far away from each other and if the same attenuation medium is considered.

Conceptionally, an exponential interaction probability, namely the probability of interaction of one photon between two points can be written

$$P(z) = 1 - e^{-\mu(\rho,E)z}, \tag{1.9}$$

in which $\mu(\rho, E)$ as previously is the linear attenuation coefficient depending on the energy E and the material density ρ. By defining an effective path length z_{eff} it is possible to do calculations by only using the well known attenuation coefficient in water $\mu_W(E)$ and equally distributed random numbers ζ in an interval (0, 1).

$$z_{eff} = -\frac{1}{\mu_W(E)} ln(1 - \zeta). \tag{1.10}$$

The main physical interactions at energies relevant for radiation therapy are

pair production and Compton effect, therefore the probability for each effect is:

$$P_{C(P)}(\rho, E) = \frac{\mu_{C(P)}(\rho, E)}{\mu(\rho, E)}. \tag{1.11}$$

A suitable algorithm for a treatment planning system (TPS) is also required to map the treatment head properly. For this the algorithm developed by Fippel et. al.[8] suggests a virtual energy fluence (VEF) model, which is based on Gaussian shaped photon distribution undergoing scattering effects in different planes coming from the source (primary scatter), the flattening filter (head scatter) and planes for 2 jaw pairs and the multi-leaf collimator. In this model the photon fluence is then calculated by integrating over the Gaussian shaped curves, resulting in a linear combination of error functions.

Another interesting algorithmic feature is the collapsed cone approximation, established by Ahnesjö et. al.[6]. It's presentation is, though, beyond the scope of this study.

Differences between PB and MC algorithms

Generally, the PB algorithm is conceptually simpler and therefore needs less computation time compared to the MC algorithm. The PB algorithm is partly based on look-up-tables and of high accuracy when dealing with rather homogeneous tissue e.g. brain regions. Bones or soft tissue is rather heterogeneous and for these regions, an improved algorithm is desired. In treatment planning this means, that PB is generally good when constructing treatment plans within the brain, but more of a problem in head and neck or the thorax region[5].

1.5 The GPR-Analysis

In clinical practice as well as in medical research, it is often of interest to compare dose distributions with each other. A method to do so, the GPR analysis, was proposed by Low et. al.[11]

It is based on a combination of the distance-to-agreement (DTA) concept and the dose deviation (DD). The former is defined as the minimum distance between a calculated point $\vec{r_C}$ and a measured point $\vec{r_M}$ of the same dose (or a defined range) in a previously defined grid. If this minimum value does not

exceed a certain distance - clinically often used values are 2 mm and 3 mm - it passes the DTA criteria. The DD criteria can be defined as percentage of a relevant dose point (or averaged conglomeration). If a difference $|D_C(\vec{r}) - D_M(\vec{r})|$ exceeds this value, the DD criteria is said to be failed. To check the dose deviation values of 2% or 3% are typically used.

The GPR-analysis is conducted by computing the formula

$$\Gamma(\vec{r}_m, \vec{r}_c) = \sqrt{\frac{(r(\vec{r}_m) - r(\vec{r}_c))^2}{\Delta d^2} + \frac{(D_C(\vec{r}) - D_M(\vec{r}))^2}{\Delta D^2}}, \tag{1.12}$$

where Δd is the previously defined distance deviation criteria and ΔD is the dose deviation criteria. Out of (1.8), the gamma index can be defined as

$$\gamma(\vec{r}_m) = \min(\Gamma(\vec{r}_m, \vec{r}_c)) \; \forall \, \vec{r}_c. \tag{1.13}$$

The GPR criterion is passed at this point if $\gamma(\vec{r}_m) \leq 1$ and failed if $\gamma(\vec{r}_m) > 1$. Finally, the actual gamma pass rate is the percentage of points passing the criteria.

Graphically the gamma criterion defines the surface of an up to 4 dimensional ellipsoid, depending on the number of spatial axes

$$\sqrt{\frac{(r(\vec{r}_m) - r(\vec{r}_c))^2}{\Delta d_M^2} + \frac{(D_C(\vec{r}) - D_M(\vec{r}))^2}{\Delta D^2}} = 1. \tag{1.14}$$

By calculating the actual gamma index in a point $\vec{r}_m$, also a spherical shape is constructed. The criteria is passed, if there is an intersection between this shape and the ellipsoid defined in (1.10).

Clinically used GPR-criteria are for example 3%/3mm or 2%/2mm. If a treatment plan is validated with these parameters, a certain predefined percentage, typically more than 90%[12], is required to make the treatment plan clinically acceptable.

A further discussion of the GPR-model, with respect to this work is given in the discussion section.

1.6 Purpose of this work

The primary purpose of this work was the investigation of dosimetric errors caused by small fields and their effect on the dose delivery quality of treatment plans with different methods and tools. Although, the theoretical foundation of these small field errors is solid, as stated in subsection 1.3, the investigation of these errors in clinical applications is not trivial. However, it is important to guarantee a sufficient accuracy in treatment planning as well as in treatment plan delivery.

A study aiming at a similar goal has already been conducted [21], indeed with some significant results. The measuring instrument used there, namely 2D a detector array system (Delta-4 phantom (ScandiDos, Uppsala, Sweden)) was limited by the coarse resolution of 5 mm near the isocenter. This created the need for a depth investigation using a measuring instrument capable of a higher resolution i.e. radiochromic films, as used in this study.

Another objective of this study was on the one hand, the systematic design of a model reflecting the errors caused by small fieds and on the other hand the correlation of this model with a GPR-analysis, resulting from the comparison of measurement and calculation.

Chapter 2

Materials and methods

The investigation of small field errors in clinical practice was performed focusing on areas of the human body treated frequently with precision radiotherapy techniques, such as Prostate, Brain and Head and Neck cancer. The study was conducted using Intensity Modulated Radiation Therapy (IMRT) and Volumetric Arc Therapy (VMAT), with a total of 34 patients and 43 different treatment plans. The plans were designed using iPlan (Brainlab, Feldkirchen, Germany) and Monaco (Elekta/CMS, Sant Louis, CA, USA), each plan with two different models for 6 MV photon beams, a clinically used one and one with altered output facotrs (OF) to account for potential small field errors. After doing so, the plans were irradiated using an Elekta Versa HD with an Elekta Agility MLC and radiochromic EBT3 films (Ashland, Covington, Ohio) served as dosimetric tool. The measurement was compared on the one hand with the plan using the clinical beam model and on the other hand the one calculated with modified OF with a GPR-analysis. Additionally, the field size distribution and the corresponding dose value per field size was calculated for each treatment plan and connected using an error model to the result of the GPR-analysis via a correlation analysis.

In RT, the dose is measured in monitor units (MU). At the Department of Radiation Oncology, Allgemeines Krankenhaus (AKH)/Medical University Vienna (MUV), according to a recommendation of the International Atomic Energy Agency (IAEA)[61] a monitor unit is defined as the dose of $1\,cGy$ in a water equivalent phantom delivered with a $10 \times 10\,\mathrm{cm}^2$ field in a depth of 10 cm and a source to surface distance (SSD) of 90 cm.

2.1 The Elekta Versa HD

The experimental part of this study was conducted using an Elekta Versa HD (Elekta, Stockholm, Sweden) with an Agility MLC, which together with Elekta Synergy linacs is part of the radiation therapy equipment at the AKH/MUV in Vienna. The Versa HD is capable of delivering electron and photon radiation, with 6 MV and 10 MV, with and without flattening filter. The MLC, which will be of major interest in this work, consists of 80 independently movable leaf pairs with a width of 0.5 cm, allowing to form an arbitrary field limiting shape within an area of nearly $40 \times 40\,\mathrm{cm}^2$.[39] Furthermore, a pair of jaws is used as beam limiting device.

Basically, degrees of freedom of the delivering device are important for the precision achieved. Not only the gantry angle of the VersaHD is flexible, but also the treatment table is equipped with 6 degrees of freedom, of which three are translational along the major axes. The treatment table can be rotated around the three axes including the axis vertically intersecting the isocenter.[42] Additionally, the Versa HD is equipped with 2 on-board imaging devices: a conebeam CT in kilovoltage range and the iViewGT in MV range.[59] These imaging systems together with the ExacTrac (Brainlab, Feldkirchen, Germany) allow versatile image-guided radiation therapy (IGRT) procedures.[60]

2.2 Outputfactors and beam models

Collecting and comparing data of OFs from different radiation facilities, showed a variation of more than 10 % for a $2 \times 2\,\mathrm{cm}^2$ field. Especially at smaller fields this variation is distinctive.[62] As discussed in more detail in section (1.3), parameters describing small fields are prone to failure, which is one of the reasons for the huge variation. However, also the inaccuracy of TPS, as far as correctly modelling small field OFs is concerned, contributes to this variation. Out of the data collected, an extrapolation can be made and in further consequence a beam model, which in comparison to the one used for clinical purposes at the AKH/MUV, contains possible errors caused by such small fields. In this case, a 6 MV FF BM was designed. A graph exemplarily showing the clinical and modified OFs as a function of the side length of the corresponding quadratic

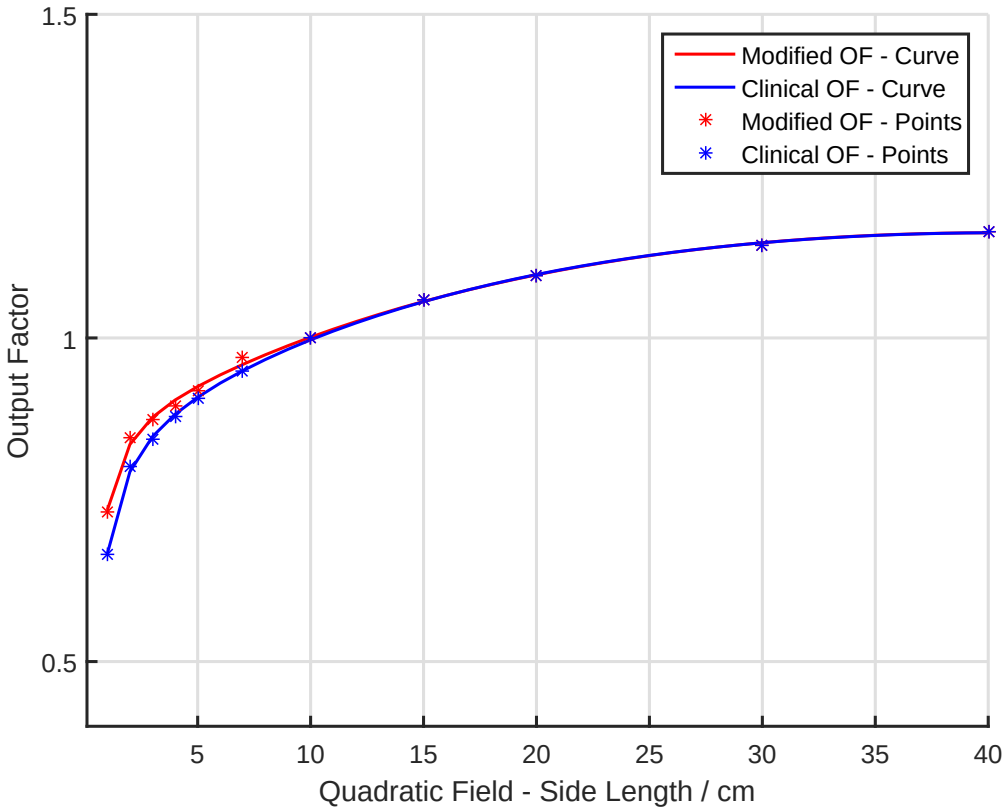

Figure 2.1: The clinical used OFs are shown together with the modified ones. Note, that the smaller the field size the more distinct is the difference between the OFs.

field, is shown in figure 2.1. These OFs are parameters of the Monaco MC algorithm.

The desired error factors resulting from the difference of OFs of clinical and modified BM are displayed in table 2.1 for iPlan (1) and Monaco (2).[21]

2.3 Treatment Planning

2.3.1 VMAT - Monaco

A set of 37 already designed VMAT treatment plans in Monaco, consisting of 12 HN plans, 16 prostate plans and 9 prostate boost plans had to be recalculated on a CT scan of the phantom, actually used for the subsequent measurements (cf. section 2.3.2). Every plan was recalculated twofold, using the clinical

Table 2.1: Summary of error factors used to construct the 6 MV FF modified beam model. The values represent quotients of the clinical and modified OFs for iPlan (1) and Monaco (2).

(1)

Edge/cm	Error factor
1	1.100
2	1.057
3	1.035
4	1.020
6	1.010
8	1.000
10	1.000
14	1.000
20	1.000
30	1.000
40	1.000

(2)

Fieldsize/cm	Error factor
1×1	1.100
2×2	1.057
3×3	1.035
4×4	1.020
5×5	1.015
6×6	1.010
7×7	1.005
8×8	1.000
10×10	1.000
14×14	1.000
15×15	1.000
20×20	1.000
30×30	1.000
40×40	1.000

beam model and the modified one as explained above. The grid for the MC simulation in Monaco was chosen to be 2 mm with a MC variance 1 % .

2.3.2 IMRT and Conformal - iPlan

The patient CT scans, as well as contours of the PTV and OAR, where exported from Monaco and imported to iPlan and IMRT plans for prostate and head & neck areas, were established using the prescriptions listed below. Additionally, 5 brain metastases treatment plans using conformal fields with a total number of 9 metastases were processed. The treatment plans were calculated with the PB algorhitm of iPlan, which is based on the publications of Mohan et al.[2–4] All prescriptions were normalized by dividing the total number of monitor units by the number of fractions. By doing so, always 2 Gy per treatment plan were irradiated, in order to be in the dynamic range of the radiochromic film.

Prostate

- Boost. 22Gy on PTV, 11 fractions

- Pelvis. 56 Gy on PTV out of which 50.4 Gy on Pelvis PTV (including ipsilateral and contralateral lymph nodes) and 5.6 Gy on Boost PTV, 28 fractions , using a simultaneously integrated boost technique

Head & Neck

- Variable Prescription. PTV from 54 up to 60 Gy and additional Boost PTV from 0 to 18 Gy, using a simultaneously integrated boost technique.

Brain metastases

- 2 Gy in 1 fraction. Beams were planned individually.

When designing the treatment plan, OAR sparing was performed according to clinical protocols. For prostate plans, the dose to OARs such as bladder, rectum and intestine and for head and neck plans, both salvary glands, myleon and brainstem were minimized as far as possible. For all treatment plans, 9 beams with uniformly distributed gantry angles were defined. For the measurement the gantry angle was set to zero degrees. The planning aim for the PTVs was to deliver a minimum of 95% of dose to 95% of the PTV volume ($V95\% > 95\%$ of PTV). For the brain metastases plans which were clinically used were investigated. With iPlan it is possible to manually choose the irradiation angle for each beam in 3 dimensions. Using these degrees of freedom, the goal of sparing OAR on the one hand and delivering a highest possible dose to the PTV on the other hand was reached. However, at least 99% of the PTV volume were aimed to be covered by 80% of the prescribed dose. The planning procedure itself was not part of this work.

Similar to the procedure described in the last subchapter, two beam models, a clinical and a modified one, were implemented in each treatment plan. Moreover, the plans were mapped on a cubic water phantom ($30\,\text{cm} \times 30\,\text{cm} \times 30\,\text{cm}$).

2.3.3 Plan and dose export

The VMAT and IMRT plans were exported twice, to the record and verify system Mosaiq (Elekta, Stockholm, Sweden) for irradiation and to obtain the

DICOM file. The latter was used to gain information about the leaf and jaw positions of the treatment head during irradiation to conduct the statistical analysis (cf. section 2.5). Secondly, dose planes corresponding to the film planes during the measurement were exported which forms the basis for the two-dimesional GPR-analysis: the plane comparison of measurement and planning system with the corresponding beam models. Finally, dose cubes for prostate cases including lymphatic targets as well as prostate boost and head & neck plans were exported from Monaco and brain metastases plans were exported from iPlan, to conduct the three-dimensional GPR-analysis using 3D Slicer, a well-known program for applications in medical physics and radiation therapy.[63–64] The entire planned dose distribution based on the clinical beam model was compared with the same plan based on the altered one.

2.4 Radiochromic films and measurement

A number of reliable dose measurement devices are commercially available, out of which radiochromic films count to the gold standard for 2D-dosimetry. They are flexible, as by cutting the films in desired sizes, it is possible to fit them easily to a variety of experimental set-ups. An additional advantage is a comparably low cost effort[23]. Furthermore, the resolution of radiochromic films is potentially up to a couple of µm depending on the scanner. However, because of their sensitiveness, the films require a careful handling. This aspect will be further addressed in the discussion section.

For the dose measurements presented in this work, Gafchromic EBT3 films manufactured by Ashland (Covington, Ohio, USA) were used. They are yellow dyed with an approximate thickness of 270 µm coming from two equally thick 120 µm matte polyester layers sandwiching a 28 µm thick active layer. The dimension of each film is 20.32 cm × 25.4 cm and in comparison to its predecessor featured with silica particles on both sides to prevent the formation of Newton rings coming from the scanning process[23].

The scanning procedure was performed with an Epson Perfection V700 scanner. As recommended by the manufacturer[23], it was sticked to a previously defined protocol. Every film was scanned prior to irradiation in order to get a suitable background field and 36 hours after irradiation in 48-bit RGB mode,

150 dpi and without using any color corrections provided by the scanner. To avoid any smear formation and to reduce dust particles at the scanner surface as much as possible, the surface of the scanner was cleaned with a propanol solution and with a fibrilar cleaning wipe. To take the scanning warm up into account, a minimum of 4 prescans were performed before starting the actual scanning procedure. With the aid of a film holder limiting the scanning area, the films could be placed exactly at the same location, which is of utmost importance when subtracting the background signals.

As the films measure dose relatively, they had to be calibrated with a suitable absolute dosimetry measuring instrument. For this purpose a Farmer Chamber 30006 manufactured by PTW (Freiburg, Germany) was used.

2.4.1 Film calibration

In order to obtain a calibration curve, 11 different films were irradiated beginning from 30 monitor units (MU) to 1600. Also these films were scanned before and after irradiation to account properly for the background.

Although the scanner provides 3 different color channels, the actual dose conversion program is only based on the red channel and therewith on single channel dosimetry, which is considered to be accurate[57]. Similar to the work proposed by Devic et al [24,50] a net optical density (OD) was calculated by

$$\text{netOD} = \log_{10}\left(\frac{I_{\text{bckg}}}{I_{\text{exp}}}\right) - \log_{10}\left(\frac{I_{\text{bckg}}}{I_{\text{unexp}}}\right), \tag{2.1}$$

in which I_{exp} and I_{unexp} are the exposed and unexposed intensity values, respectively, and I_{bckg} represents the intensity value at which zero light is transmitted. At a 48-bit mode using red channel this is $2^{16} = 65536$.

In order to assign the amount of Gray irradiated to the net OD, which is the actual goal of calibration, the PTW Farmer Chamber 30006 was used. Having the ion chamber placed under 10 cm of solid water layers, 200 MU were irradiated 3 times and after multiplying the detector output in Coloumb with suitable factors accounting for beam energy, polarization and recombination effects, temperature and pressure and the chamber's calibration coefficient, the mean value in Gray could be obtained. The output gathered by multiplying

these factors is justified by the Bragg-Gray theory. Finally, a fourth degree polynomial fit function was constructed and implemented in a previously designed MATLAB code. Hence, it was possible to allocate an arbitrary net OD value to an actual dose value.

2.4.2 Measurement procedure

The entire measurement procedure was conducted using an Elekta Versa HD linac with an Elekta Agility MLC. In order to prepare the treatment plans for measurement, they were sent to Mosaiq, the record and verify system utilized at the Department of Radiation Oncology. Overall, 37 VMAT plans, 37 IMRT and 5 conformal field plans were irradiated.

In order to measure IMRT plans, a film was placed on the table in the coronal plane between solid water plates (Sun Nuclear, Melbourne, Australia), as can be seen on the right of figure 2.2. The film was put in a depth of $10\,cm$ and having a $15\,cm$ solid water layer at the bottom side, to account for backscatter. Although the concept of plane matching, as described below does not use the isocenter itself, it was marked on the edge of every film, to allow for a double check. IMRT treatment plans were delivered with gantry angle of zero degree.

For the corresponding VMAT plans, the film was placed in the transversal plane in the phantom depicted on the left of figure 2.2. This phantom is in-house developed consisting of removable polystyrene plates. For the measurements, the isocenter was chosen between two polystyrene plates, sandwiching the film.

Finally, plans delivering conformal fields for the treatment of brain metastases, as outlined above, were irradiated. For these measurements, the same settings as for IMRT plans were applied.

The reason why two different phantoms were used, simply lies in the fact, that iPlan mostly works with a pencil beam algorithm, as introduced in section 1.4.1. This algorithm tends to show greater uncertainties at inhomogeneous materials and difficulties could occur, when the beam enters from an oblique angle. Therewith, the use of homogeneous solid water plates was motivated.

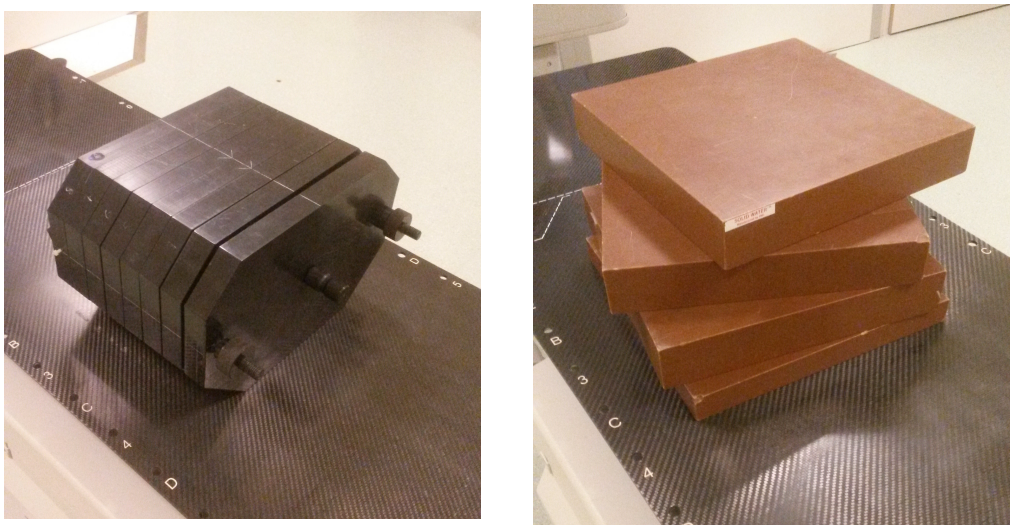

(a) **(b)**

Figure 2.2: VMAT plans were delivered using a inhouse-made phantom (a) and IMRT was measured with the aid of solid water plates (b).

2.5 Evaluation procedure

2.5.1 Three-dimensional GPR-analysis using 3D Slicer

The first evaluation was made using 3D Slicer, a open source toolkit for applications in radiotherapy. This program contains a number of useful tools, one of which, the three-dimensional GPR-analysis was used to compare the plan based on the clinical beam model with the plan based on erroneous OFs. For this purpose, the three-dimensional dose matrix, extracted previously for each plan from Monaco was used. Only the brain metastases plans were exported from iPlan.

Overall, a gamma criterion of 3 %/3 mm was applied and only dose values exceeding 10% of the maximum dose were considered. A dose difference criteria of 3 % was taken by default from the maximum dose.

3D Slicer is also capable of drawing a three dimensional gamma map, which is a color code indicating gamma values. This is valuable tool and allows further localization and interpretation of spots with low GPR-values, as discussed in section 4.2. These spots were analyzed statistically by empirically allocating numbers i.e. 1 corresponding to 'barely noticable' up to 4 corresponding to

'very significant'. The numbers representing the intensity were used to conduct a correlation analysis by Spearman[46–47], as explained in section 2.7.

2.5.2 Evaluation of film measurements

The MATLAB code converting the netOD to dose has a graphical user interface (GUI), allowing to directly upload the data in tagged image file format (tif), obtained from the scanner. One of the features of this dose evaluation program is an implemented correction for lateral scanning inequalities. This is a well known phenomenon[23,42], which can be avoided when dealing with small films by simply placing them in the center of the scanner. However, the measurements presented here make use of full sized films and therefore the entire scanning area within a film holder had to be used and the values had to be corrected correspondingly.

The Matlab code generates a dose grid using the calibration curve mentioned in section 2.3.1. Although the scanning resolution was 150 dpi, the evaluation program generates a grid with a distance of 1 mm between each entry, which corresponds to the maximum resolution of the planning software (Monaco and iPlan) when exporting a plane. This matrix was then saved as text file.

2.5.3 Data matching

When considering the calculated and measured dose plane, the question of how to correctly overlay both planes arises. This is important for the comparison, as the final result of the GPR-analysis highly depends on the superposition quality.

In order to solve this problem, a MATLAB code using two different matching approaches was written:

Firstly, the maximum of each row and column for both matrices was calculated giving two one dimensional arrays for each matrix. By discretely calculating the convolution of the column maxima for each matrix, the correct coordinates for the overlap in one dimension can be found by requiring, that the difference is minimal when the columns are superposed correctly. The coordinates of superposition along the other axis can be found analogously by calculating the

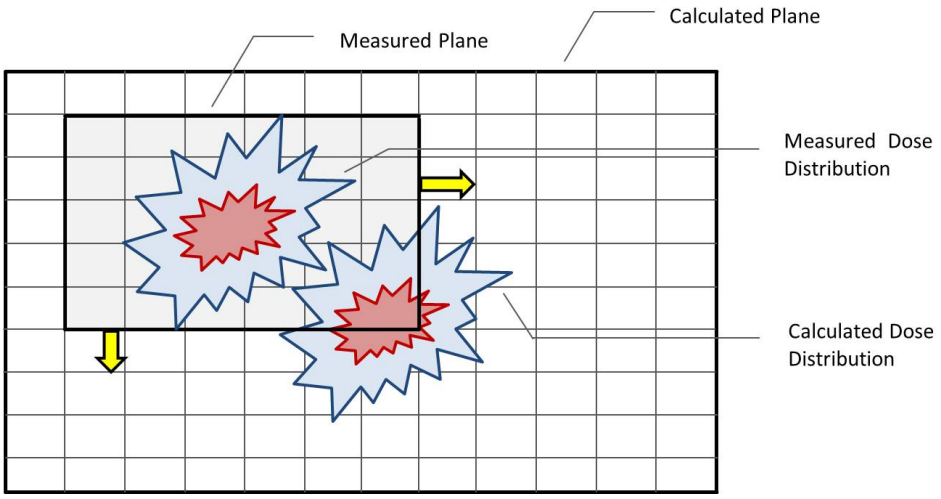

Figure 2.3: The measured plane is computationally displaced relative to the calculated plane, as indicated by the yellow arrows. The dose difference of both planes for every possible overlap is computed. The proper overlap is found by minimizing the dose difference between the planes.

difference of the row maxima.

The second approach makes use of the same concept in a two dimensional way. As the matrix containing the calculated data is usually bigger than the measured one, the latter is cropped to the same size, but with an alternating number of rows and columns at the front and back. With this technique the difference was calculated for every possible superposition of the matrices. Again the minimum was taken in order to find the correct coordinates. A sketch outlining this procedure is pictured in figure 2.3.

The two-dimensional matching procedure was found to have a higher accuracy, as it is not so sensitive to dose fluctuations occurring at some pixels than compared to the first method introduced. However, mostly both techniques showed the same result. The methods work well if the difference of the planes to be matched is expected to be small. Furthermore the data in each matrix must not be too uniformly distributed, i.e. the gradients must be sufficiently steep. All requirements were fulfilled by the matrices to be matched. The second approach takes considerably more CPU time, but for the used matrix sizes still less than a minute.

2.5.4 GPR-analysis based on film measurements

The matched matrices were then compared using a two dimensional GPR-analysis. For this purpose, two Matlab codes were used, one downloaded from the internet with a GUI and a in-house developed one, to allow a comparison. Generally, the 3%/3 mm criteria was applied and only points with a dose value higher or equal to 20% of the maximum dose were considered. Furthermore, the GPR-analysis was conducted using the DD percentage of the global maximum of the calculated matrix.

It was strictly focused on using exactly the same parameters for each treatment group when conducting the GPR-analysis. Otherwise, the results would not be comparable and the result of the statistical correlation analysis conducted afterwards would be distorted. However, when comparing VMAT plans with GPR-analysis, the distance between each point was decreased by a factor 0.2 respectively, compared to the IMRT plans. In other words the resolution of the matrix was fivefold increased, resulting in an up-scaled GPR. As mentioned above, this can be justified by the fact, that it was done equally for all constituent plans within a treatment group and therefore the basic trend, if existing, would naturally be conserved. The reader is referenced to section 4.5 in which this aspect is addressed in greater detail.

2.6 Analysis of field sizes and error modelling

A further goal of this work was the correlation of occurrence of small fields during a treatment plan with the previously calculated GPR values. For the extraction of field sizes or aperture lengths, respectively, a Matlab code was written, using the previously exported treatment plans in dicom-format as input. These files contain the positions of each leaf pair for each control point as well as the jaw positions for each control point. The coordinates are extracted and leafs behind the jaws were not considered, as they do not contribute to the dose distribution.

This code was written for the treatment plans of an Elekta VersaHD. Little changes would have to be made to guarantee applicability for an Elekta Synergy, as they have an additional jar pair implemented. The code can handle

four different treatment types: sas IMRT, dynamical IMRT, conformal beams and VMAT. However, sas IMRT plans were not part of this study. The mayor difference for this program between dynamical and statical (sas) leaf sequencing lies in its calculation of the mean field size between two control points. For dynamical leaf sequencing, the leafs change continuously, so a linear interpolation is appropriate to calculate the mean field size. Then, a steady shift velocity of each leaf is assumed. However, not dynamical sequenced leaf positions remain static over the duration between two control points, which therefore do not need an interpolation.

The distribution of apertures for a treatment plan can be characterized in two different ways to make a further study possible. Firstly, the frequency distribution of aperture lengths can be displayed. Secondly, the distribution weighted by the amount of MUs irradiated by each field size can be mapped. For this illustration, the leaf aperture length was multiplied with the leaf width giving an area. Then, the overall irradiated MUs between 2 control points were allocated to this areas, assuming equally distributed dose over the entire MLC plane. For display, a histogram with variable resolution and axis lengths was chosen.

Error modelling

For simulating the error caused by the occurrence of small fields and constructing a consistent error model, the following assumptions were made:

- The entire model is based on the error factors reflecting the variation of OFs caused by small fields, which are presented in table 2.1. This implicitly means, that the calculated error for a leaf configuration must be equal to the corresponding entry in table 2.1, if the field sizes are equal.

- It is possible to deduce the error of an arbitrary rectangular field from the error of one or more quadratic fields. For instance, considering a $2 \times 1\,\mathrm{cm}^2$ field, the error would equally be contributed by a $1 \times 1\,\mathrm{cm}^2$ field (representing the short distance between opposing sides) and a $2 \times 2\,\mathrm{cm}^2$ field (representing the long distance between opposing sides). Considering table 2.1, the error in this case would be: $1 + (1 - \frac{1.1+1.057}{2}) = 1.0785$

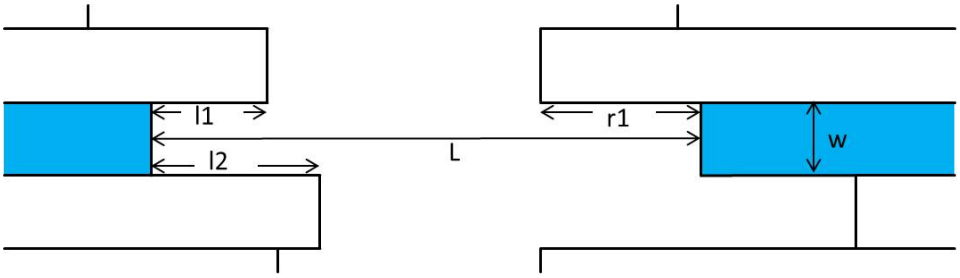

Figure 2.4: The geometry of leaf positions to facilitate the understanding of equations (2.3)-(2.7) is shown.

- Furthermore a more complex two dimensional shape, which occurs as a result of the (potentially arbitrary) leaf positions for 80 leaf pairs during a treatment plan can be deduced from the error factors of quadratic fields, by considering each length of the shape as linked to the corresponding quadratic field side length.

The last point from above, indicates the need for a fitting curve, with which errors of quadratic fields with every desired side length can be recalled. The best fitting curve was obtained using

$$a\, e^{-\frac{b}{x}} + c\, e^{\frac{d}{x}} + \frac{e}{x+1}, \tag{2.2}$$

with a, b, c, d and e being parameters to be determined. Finally, after implementing the model with its assumptions in a MATLAB code, a value between 1, corresponding to no error, up to a certain threshold value (defined by the user), defining the maximum error represents an indicator for small field errors during the treatment plan irradiation. The implementation of the threshold will be further addressed and justified in the following sections.

A graphical outline of the leaf geometry is given in figure 2.4. Consider the leaf pair marked in blue and let ErFit be the fitting curve shown in (2.2), than the error for the upper side of the leaf pair can be calculated by using the ratios

$$\mathrm{ErrorUp} = \frac{\mathrm{l1}}{\mathrm{L}}\,\mathrm{ErFit(l1)} + \frac{\mathrm{r1}}{\mathrm{L}}\,\mathrm{ErFit(r1)} + \frac{\mathrm{L}-\mathrm{l1}-\mathrm{r1}}{\mathrm{L}}. \tag{2.3}$$

The error value caused by the length l1 is obtained from the fitting curve. This is according to the third point itemized, namely, that the error factors

of quadratic fields correspond to its field limiting lengths. As the output should only be a factor between 1 and a certain threshold, the error values must be normalized. The normalization is represented by dividing by L. This implicitly means, that an error factor for a small field is bigger according to the fitting curve, but by normalization it will be scaled and gets smaller, which is considered to be justified, as a smaller length also can influence a smaller part of the whole field. The last term in (2.3) is a ratio representing the open part of the upper side (cf. figure 2.4), to which no error is allocated. Analogously, the lower side in figure (2.4) can be expressed

$$\text{ErrorLow} = \frac{\text{l2}}{\text{L}}\,\text{ErFit(l2)} + \frac{\text{L} - \text{l2}}{\text{L}}. \tag{2.4}$$

In this case, there is no leaf limiting the field at the lower right side, so one term vanishes compared to the upper side. Furthermore the vertical length on the left can be expressed as simply

$$\text{ErrorLeft} = \text{ErFit(w)}. \tag{2.5}$$

For the right hand side, the lack of field limiting on the lower side is modelled by taking the average between the error caused by the vertical length w and no error

$$\text{ErrorRight} = 1 + \frac{1 - \text{ErFit(w)}}{2}. \tag{2.6}$$

Finally, a parameter denoting the error caused by the absolute distance of the gaps L, must be introduced, leading to the fifth and last part of the model.

$$\text{ErrorGap} = \text{ErFit(L)}. \tag{2.7}$$

Averaging of equations (2.3)-(2.8) can be used to calculate an error factor for all leaf pairs and all control points of a treatment plan. The dynamical leaf sequencing must not be neglected and was also implemented in the model.

The desired result is one factor for a plan indicating the error caused by small fields during the entire treatment plan irradiation.

2.7 Statistical Methods

One of the goals of this study, was the correlation of GPR results with the error factors generated by the error model. In this context, it was of interest to investigate, if there was a monotonic function between these set of values. For that reason, a correlation coefficient analysis by Spearman was considered to be appropriate.[46–47] Generally, the indicator of the monotonical correlation, $\rho_{Spearman}$ can have values between -1, indicating a perfectly monotonically decreasing correlation and 1, indicating the corresponding monotonically increasing trend between two sets of variables. An advantage of this analysis compared to the widely used correlation analysis by Pearson, is that it does not need the underlying assumption of linearity between the set of variables. Spearman's coefficient is said to be expressive, only if the corresponding p-value, which is the value indicating the statistical significance, is below a previously defined threshold. In this study, the threshold of the p-value is set to be $\alpha = 0.05$.

Another analysis was conducted to correlate the GPR based on the modified BM with the one based on the clinically used BM. The scope in this case differs from the analysis described above, as it is not primarily of importance to investigate a potential function between the sets of values, but rather examine if there is a trend of one set to have generally higher or lower values. In this case, a two-paired Student's t-test was considered to be appropriate.[48] Also for this test a significance level of $\alpha = 0.05$ was chosen as a threshold.

Both correlation analyses were conducted using Matlab routines.

Chapter 3

Results

3.1 Film calibration

To obtain reliable measurement results, an accurate film calibration is vital. This justifies a careful examination and extended effort to achieve accurate results, which is the reason, why the calibration process was done twice to investigate the variation and reproducibility. For both calibrations and each film, the obtained scanner raw values after irradiation I_{exp} as well as the background values before measuring I_{unexp} and the corresponding net OD values, calculated with formula (2.1), are shown in table 3.1. In order to obtain the raw values, a region of interest (ROI) for each film of about $3 \times 3\,\text{cm}^2$ was averaged. The comparison of the net ODs has shown a good agreement, as can be seen in the last column of table 3.1. All deviations are below 2%, which is within the expected error range of approximately 5 %. The highest deviations can be found at MU values of 200 and 400, respectively, with percentages slightly less than 2%. The mean deviation of the net ODs is 1.08 %. For the evaluation procedures, it was continued with the most recent calibration.

Table 3.1: Measured scanner raw values before I_{unexp} and after I_{exp} irradiation and calculated net OD values for both calibration procedures. In the last column, the deviation in per cent is given.

Nr	MU	first calibration			second calibration			Deviation
		I_{unexp}	I_{exp}	net OD	I_{unexp}	I_{exp}	net OD	net OD
0	0	39604	39604	0	39707	39707	0	0 %
1	30	39590	36809	0.0316	39099	36360	0.0315	−0.28 %
2	50	39650	35136	0.0525	39166	34750	0.0520	−1.02 %
3	100	39664	31710	0.0972	38960	31183	0.0967	−0.52 %
4	150	39799	29058	0.1366	38982	28471	0.1365	−0.10 %
5	200	39092	26480	0.1692	39735	26711	0.1725	1.92 %
6	400	39201	20660	0.2782	39233	20414	0.2837	1.96 %
7	600	39117	17281	0.3548	39138	17119	0.3591	1.20 %
8	800	39229	15183	0.4122	39017	14877	0.4187	1.55 %
9	1000	39205	13555	0.4612	39230	13350	0.4681	1.47 %
10	1300	39000	11912	0.5151	39103	11765	0.5216	1.26 %
11	1600	39085	10857	0.5563	39309	10838	0.5596	0.58 %

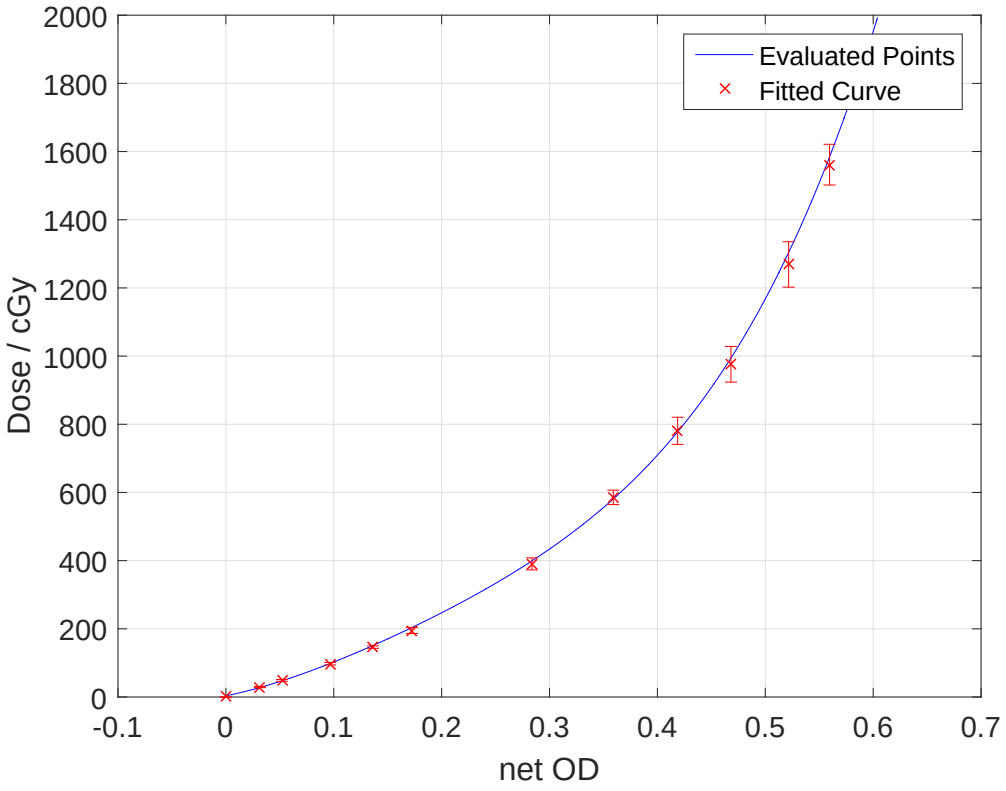

Figure 3.1: Plot of the calibration curve used to calculate the dose. The conversion of net OD into the actual dose was made using a fourth degree polynomial fitting curve.

3.2 Three-dimensional GPR-analysis using 3D Slicer

The evaluation with Slicer was a rather straightforward procedure. For prostate with lymph nodes (Pr-ln), prostate boost (Bo), head & neck (HN) and brain metastases (Br) treatment plans the results of the GPR-analysis including mean GPR and standard deviation per treatment group are presented in table 3.2.

Except for the brain metastases plans, all mean GPR values were above 99 %, whereas boost plans have the highest mean GPR of 99.7 %, closely followed by prostate with lymphatic pathways plans with a mean of 99.9 %. Finally, for head and neck plans an averaged gamma pass rate of 99.3 % was calculated. Besides the high mean GPR for prostate boost, prostate with lympatic pathways and head and neck plans, the calculated standard deviation is below 0.3 %, ranging from 0.2 % for prostate with lymphatic pathway plans to 0.3 % for head and neck plans. Compared to the other treatment groups in table 3.2, brain metastases have a conspicuous low mean GPR. Furthermore they have a nearly ten times higher standard deviation compared to the mean standard deviation for the other three treatment groups.

3.3 Irradiation of plans using Mosaiq

During the irradiation process, VMAT plans frequently caused an error notification, informing the user about the dose rate, falling below a threshold implemented in the linac. This caused the VersaHD to stop delivering dose, but after resetting the MU counter and with the aid of Mosaiq, it was possible to continue the measurement from the point it stopped. This notification usually occurred once or twice per irradiated plan and only affected VMAT plans.

Furthermore it was noticed, that for setup reasons, Mosaiq did not allow the irradiation of a number of IMRT beams. However, the linac settings and software itself had no problem with irradiating these beams and therefore they were delivered using the service mode of the linac software.

Table 3.2: Three-dimensional GPR resulting from the comparison of plans based on the clinical BM with ones based on a modified BM using 3D Slicer. Displayed are comparisons for head and neck plans (1), prostate boost plans (2), brain metastases plans (3) and prostate with lymphatic pathways plans (4).

(1)

Patient	GPR-Value
Br1	98.2%
Br2	97.8%
Br3	100.0%
Br4	100.0%
Br5	99.9%
Br6	92.6%
Br7	97.1%
Br8	96.8%
Br9	95.4%
MEAN	97.5%
STD	2.5%

(2)

Patient	GPR-Value
Bo1	99.9%
Bo2	99.6%
Bo3	99.7%
Bo4	99.9%
Bo5	99.9%
Bo6	100.0%
Bo7	99.5%
Bo8	99.7%
Bo9	99.2%
MEAN	99.7%
STD	0.2%

(3)

Patient	GPR-Value
HN1	99.3%
HN2	98.6%
HN3	99.4%
HN4	99.5%
HN5	99.3%
HN6	99.4%
HN7	99.2%
HN8	99.5%
HN9	99.4%
HN10	99.5%
HN11	99.4%
HN12	98.8%
MEAN	99.3%
STD	0.3%

(4)

Patient	GPR-Value
Pr-ln1	99.7%
Pr-ln2	99.6%
Pr-ln3	99.5%
Pr-ln4	99.7%
Pr-ln5	99.8%
Pr-ln6	99.7%
Pr-ln7	99.8%
Pr-ln8	99.9%
Pr-ln9	99.9%
Pr-ln10	99.2%
Pr-ln11	99.7%
Pr-ln12	99.6%
Pr-ln13	99.8%
Pr-ln14	99.4%
Pr-ln15	99.2%
Pr-ln16	99.9%
MEAN	99.7%
STD	0.2%

3.4 GPR-analysis based on film measurements

With the parameters mentioned in section 2.5.4, the GPR-analysis was conducted for IMRT as well as for VMAT plans. The measured planar dose distribution was compared to the clinically used beam model and to the one with modified OFs. The summarized results for all four treatment groups, together with the mean GPR value and its standard deviation are summarized in table 3.3 and table 3.4. For brain metastasis in table 3.3 (1), not only the ratio of calculated dose based on clinical BM and modified BM is given, but also the dose ratio of calculated clinical BM to measured dose and modified BM to measured dose. All dose values were extracted from the isocenter. As far as IMRT plans calculated with iPlan are concerned, there was no difference found between the exported dose matrices based on the clinical used OFs and the modified ones. This is the reason why table 3.3 and 3.4 show only one column for IMRT. After a first suspicion caused by identical GPR, this was found out by simply calculating the deviation of the calculated matrices based on both BMs.

The brain metastases have very similar GPR for both BM as shown in table 3.3 (1). The GPR based on the clinical BM and the result on the basis of the modified BM were basically equal with 99.4 %. Also the standard deviations were found to be equal with 0.5 % and 0.5 % for the clinical and modified BM, respectively. When considering the dose ratios, especially the ratios based on calculated clinical BM to measured dose value in the isocenter is remarkable, as for all brain metastases plans, that ratio is below 1. However, all mean ratios are below 1 ranging from 0.95 to 0.97.

The calculated GPR for IMRT and VMAT prostate boost plans show mean values above 95 %, but definitely below the values for brain metastases plans. A trend of higher mean GPR for IMRT with 98.4 % compared to 95.8 % and 96.5 %, respectively, is clearly visible for VMAT. However, the standard deviations are very similar with IMRT having the highest deviation of 2.3 % and VMAT having 2.1 % and 2.2 % for clinical and modified BM respectively.

The above mentioned trend of a higher GPR for prostate boost IMRT plans compared to VMAT plans is not continued for the head & neck treatment group as shown in table 3.4 (1). This group shows a mean GPR of 95.7 %

Table 3.3: The results of the GPR-analysis for brain metastases plans (1) and prostate boost plans (2) based on the comparison of measured planar dose distribution and calculated planar dose distribution using the clinical beam model (clin BM) and the modified beam model (mod BM) are shown. Additionally (1) shows the dose ratio of clinical BM to modified BM, clinical BM to measured BM and modified BM to measured BM in the isocenter.

(1)

Patient	GPR-value Conformal		Dose Ratios		
	clin BM	mod BM	clin BM / mod BM	clin BM / meas	mod BM / meas
Br1	99.8%	99.9%	0.96	0.96	1.00
Br2	99.3%	99.6%	0.96	0.96	1.00
Br3	98.8%	98.7%	1.00	0.90	0.90
Br4	98.3%	98.3%	1.00	0.92	0.92
Br5	99.7%	99.7%	0.99	0.96	0.96
Br6	100.0%	99.6%	0.94	0.92	0.98
Br7	99.9%	99.8%	0.95	0.97	1.02
Br8	99.7%	99.6%	0.95	0.96	1.01
Br9	99.6%	99.5%	0.94	0.97	1.03
MEAN	99.4%	99.4%	0.97	0.95	0.98
STD	0.5%	0.5%	0.02	0.02	0.04

(2)

Patient	GPR-value		
	IMRT	VMAT	
		clin BM	mod BM
Bo1	95.0%	96.3%	95.8%
Bo2	99.9%	94.9%	95.8%
Bo3	99.2%	95.1%	97.2%
Bo4	93.7%	98.6%	99.0%
Bo5	99.6%	93.1%	92.2%
Bo6	99.5%	92.2%	94.1%
Bo7	99.6%	97.1%	97.8%
Bo8	99.4%	97.6%	98.2%
Bo9	99.5%	97.3%	97.9%
MEAN	98.4%	95.8%	96.5%
STD	2.3%	2.1%	2.2%

Table 3.4: The results of the GPR-analysis for head and neck plans (1) and prostate with lymphatic pathways plans (2) based on the comparison of measured planar dose distribution and calculated planar dose distribution using the clinical beam model (clin BM) and modified beam model (mod BM) are shown.

(1)

Patient	GPR-value		
	IMRT	VMAT	
		clin BM	mod BM
HN1	95.8%	97.2%	97.8%
HN2	90.0%	96.8%	98.4%
HN3	97.4%	95.8%	96.4%
HN4	95.3%	97.9%	98.6%
HN5	97.0%	92.0%	92.4%
HN6	97.2%	99.4%	99.7%
HN7	91.1%	98.1%	98.3%
HN8	98.2%	99.1%	99.1%
HN9	92.8%	97.5%	97.6%
HN10	99.1%	98.0%	97.4%
HN11	97.2%	95.4%	96.0%
HN12	97.5%	97.7%	97.6%
MEAN	95.7%	97.1%	97.4%
STD	2.9%	2.0%	1.9%

(2)

Patient	GPR-value		
	IMRT	VMAT	
		clin BM	mod BM
Pr-ln1	97.1%	98.5%	99.2%
Pr-ln2	87.4%	99.5%	99.7%
Pr-ln3	98.1%	97.3%	98.6%
Pr-ln4	86.3%	99.8%	99.8%
Pr-ln5	98.2%	95.4%	98.1%
Pr-ln6	99.3%	97.7%	98.0%
Pr-ln7	99.5%	92.8%	89.8%
Pr-ln8	89.0%	94.3%	95.6%
Pr-ln9	96.3%	96.8%	98.5%
Pr-ln10	85.6%	94.4%	95.2%
Pr-ln11	94.4%	97.6%	97.2%
Pr-ln12	97.8%	90.1%	94.1%
Pr-ln13	95.4%	98.4%	99.4%
Pr-ln14	99.0%	96.1%	97.6%
Pr-ln15	99.0%	99.2%	98.8%
Pr-ln16	96.2%	96.6%	98.2%
MEAN	94.9%	96.5%	97.4%
STD	4.9%	2.6%	2.6%

Table 3.5: The results of t-test, including p-value, degrees of freedom and t_{stat} for each treatment group are displayed.

Patient Group	p-value	degrees of freedom	t_{stat}
Pr-ln	0.042	15	-2.23
Bo	0.077	8	-2.03
HN	0.035	11	-2.40
Br	0.790	8	0.27

in contrast to values of 97.1 % and 97.4 % for VMAT plans based on clinical and modified BM respectively. However a definite similarity of both treatment groups is the higher GPR for the modified BM compared to the clinical BM. As far as the head & neck treatment group is concerned, the standard deviation of 2.9 % for IMRT plans is significantly higher than the ones for VMAT, both values beeing slightly below 2 %.

The prostate cases including lymph targets have the lowest mean GPR for IMRT plans with 94.9 % and the highest standard deviation of 4.9 %. In this group there is furthermore a number of 4 plans showing GPR lower than 90 %. The VMAT GPR for both BM is higher with 96.5 % for the clinical BM and 97.4 % for the modified BM. On average, also this treatment group follows the trend of a higher VMAT GPR for the modified BM.

The results of the two-paired t-test, motivated in section 2.7 and conducted to find out eventual significances of the values given in table 3.3 and 3.4 are shown in table 3.5. Two treatment groups, namely prostate with lymph nodes and head & neck indeed show a correlation, yielding p-values below the threshold of 0.05. The trend of the correlation for these treatment groups is, as indicated above, a higher GPR for calculated dose distributions based on the modified beam model.

3.5 Analysis of field sizes and error modelling

After exporting each treatment plan from Monaco and iPlan respectively, they were integrated in the Matlab code described in section 2.5. So, the leaf positions and in further consequence the leaf apertures for all leaf pairs, mapped with a histogram were obtained. Examples of this output are given in figure

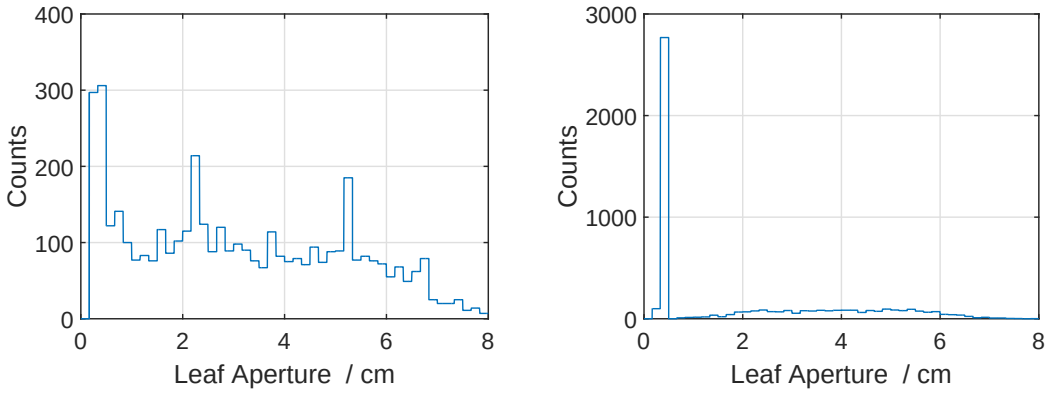

Figure 3.2: Leaf aperture distribution for a boost plan from iPlan (IMRT) (a) and Monaco (VMAT) (b).

3.3 and 3.4 for one boost plan extracted from both iPlan and Monaco. Figure 3.3 shows the leaf aperture distribution by counts and figure 3.4 shows this distribution weighted with the corresponding amount of MUs irradiated. Note that figure 3.3 and 3.4 shows only an IMRT plan calculated by iPlan and a VMAT plan calculated by Monaco of the same patient. The difference in leaf aperture is caused by the respective software and treatment type used system used.

In figure 3.5 the leaf aperture distribution for a brain metastases plan using conformal field extracted from iPlan is shown. There are no counts for leaf gaps exceeding 3.5 cm, which is caused by the rather small geometry of brain metastases. Additionally, the counts are significantly lower, as the leaf configuration does not change within a beam. In the illustrated case, 2 brain metastases were irradiated with a total of 19 beams.

Error Modelling

According to the basics and assumptions of the error model based on the factors presented in table 2.1 and explained in detail in section 2, error factors were generated. This output is summarized and tabularized for each plan including standard deviation and mean value for each treatment group in table 3.6. Sometimes, one treatment plan contains more treated areas as it is the case when treating brain metastases. As can be seen in table 3.6 (1), the first 2 and the last 3 brain metastases correspond to one treatment plan.

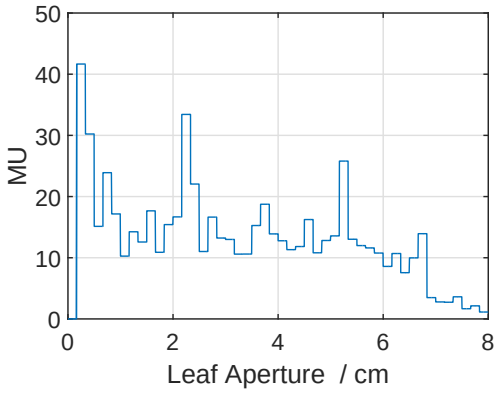

(a) IMRT: 596 MU irradiated in 187 control points

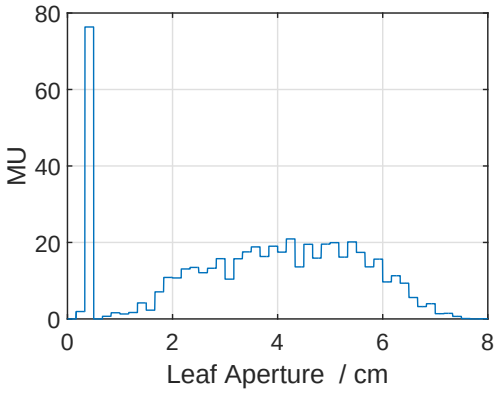

(b) VMAT: 513.8 MU irradiated in 99 control points

Figure 3.3: Leaf aperture distribution weighted by MUs for a boost plan from iPlan (IMRT) (a) and Monaco (VMAT) (b). Displayed are MUs irradiated through the corresponding rectangular areas caused by each leaf gap.

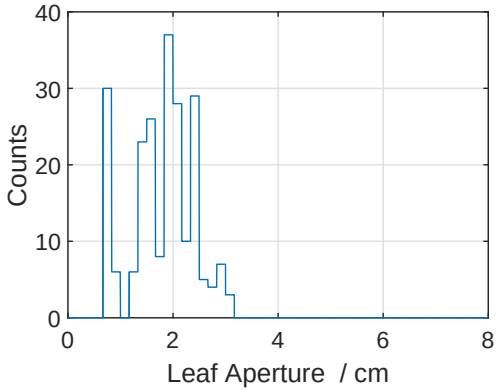

(a)

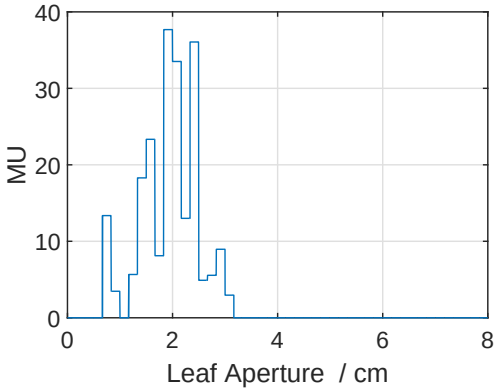

(b)

Figure 3.4: Leaf aperture distribution for a brain metastases plan using conformal fields from iPlan by count (a) and weighted with irradiated amount of MU (b).

For IMRT plans, calculated with iPlan, the lowest mean error factor was 1.049 found at prostate boost plans and the highest was 1.060 for prostate with lymphatic pathways plans. Head & neck IMRT plans were in the lower middle of these values with an error factor of 1.052. The standard deviation was equal 0.003 for both IMRT prostate treatment groups and with 0.004 slightly higher for IMRT head & neck. It is clearly visible in table 3.6, that VMAT plans overall have a higher mean error factor and also a slightly higher standard deviation, except head & neck, where IMRT and VMAT standard deviations are equal. However, comparing all VMAT treatment groups, the prostate boost group showed the highest mean error of 1.084 followed by head & neck with 1.083 and prostate with lymphatic pathways having the lowest mean error with 1.080. Finally, conformal field brain metastases treatment plans have error factors comparable with IMRT factors with a mean error factor of 1.057. The standard deviation is the highest of all treatment groups with 0.007.

Field Size Correlation

As mentioned previously, it is one of the mayor goals in this work, to statistically correlate the GPR to the previously calculated error factors. If the results of the GPR-analysis are mainly influenced by small field errors, and the calculated error factor are a proper indicator for such distortions, there should be a indirect proportional correlation, meaning a plan with lower GPR should have a higher error factor.

In order to quantify this presumed correlation, a rank correlation analysis according to Spearman [46,47] was conducted. $\rho_{Spearman}$ as well as the corresponding p-value are summarized in table 3.7. For brain metastases, only plans in iPlan were available. As table 3.7 shows no p-value falls below the threshold given by α. Brain metastases plans were only designed in iPlan.

Table 3.6: Error factors generated by the leaf model described in section 2 for VMAT and IMRT are summarized for brain metastases (1), prostate boost (2), head and neck (3) and prostate with lymphatic pathways (4).

(1)

Patient	Error Factor
	Conformal
Br1	1.058
Br2	
Br3	1.051
Br4	1.065
Br5	1.046
Br6	1.062
Br7	1.060
Br8	
Br9	
MEAN	1.057
STD	0.007

(2)

Patient	Error Factor	
	IMRT	VMAT
Bo1	1.051	1.080
Bo2	1.053	1.085
Bo3	1.048	1.081
Bo4	1.052	1.078
Bo5	1.046	1.089
Bo6	1.052	1.084
Bo7	1.046	1.095
Bo8	1.048	1.082
Bo9	1.047	1.078
MEAN	1.049	1.084
STD	0.003	0.006

(3)

Patient	Error Factor	
	IMRT	VMAT
HN1	1.050	1.085
HN2	1.056	1.081
HN3	1.053	1.071
HN4	1.058	1.085
HN5	1.048	1.082
HN6	1.053	1.082
HN7	1.051	1.084
HN8	1.045	1.083
HN9	1.051	1.083
HN10	1.049	1.085
HN11	1.057	1.084
HN12	1.054	1.086
MEAN	1.052	1.083
STD	0.004	0.004

(4)

Patient	Error Factor	
	IMRT	VMAT
Pr-ln1	1.059	1.076
Pr-ln2	1.060	1.079
Pr-ln3	1.065	1.081
Pr-ln4	1.065	1.079
Pr-ln5	1.059	1.080
Pr-ln6	1.060	1.078
Pr-ln7	1.053	1.082
Pr-ln8	1.060	1.077
Pr-ln9	1.058	1.080
Pr-ln10	1.057	1.091
Pr-ln11	1.062	1.078
Pr-ln12	1.059	1.076
Pr-ln13	1.062	1.084
Pr-ln14	1.061	1.076
Pr-ln15	1.063	1.080
Pr-ln16	1.061	1.074
MEAN	1.060	1.080
STD	0.003	0.004

Table 3.7: Statistical correlation between calculated error factors and results of the GPR-analysis (comparison of the film measurements with clinically used beam model). Spearman's ρ and the corresponding p-value indicating the significance for each treatment group are given below.

Treatment Group	IMRT - iPlan		VMAT - Monaco	
	$\rho_{Spearman}$	p-value	$\rho_{Spearman}$	p-value
Pr-ln	-0.149	0.583	0.078	0.774
Bo	0.183	0.644	-0.567	0.121
HN	-0.329	0.297	0.189	0.558
Treatment Group	Conformal Fields			
	$\rho_{Spearman}$		p-value	
Br	-0.149		0.583	

Chapter 4

Discussion

It is of special interest to examine the reliability of the result and to find and analyze possible error sources, as done in this section in addition to interpreting the results and benchmarking them against the literature.

4.1 Film calibration

Radiochromic films are a state-of-the-art and reliable dose measurement tools. However, they tend to be sensitive to variations in evaluation procedure, contaminations, variations in manufacturing (i.e. unequal thicknesses) and light, to name just a few. When the calibration procedure and the averaging over a ROI was done, it was observed, that a considerable standard deviation between 100 and 180 raw value units can occur. This is especially significant at lower dose levels, as it can cause variations up to 3% of the mean value, which needs to be considered as a potential source of error. Although, the scanning process was done carefully, dust particles are unavoidable on the film, but are considered to barely contribute to the overall dosimetric uncertainty. A more plausible reason for this standard deviation is the central depression effect, namely a slightly decreased dose rate and therewith lower overall dose in the center of the field, caused by flattening filters. This was indeed seen by plotting the profile of the raw value distribution of a number of film pieces used for calibration (results not shown). The effect is suggestively illustrated in figure 1.1a, see introductory section. Additionally, the standard deviations

were found to be higher in areas of low dose. This can be attributed to the nonlinearity in response of the film.

In order to allocate scanner raw values to dose, different fitting models can be found in the scientific literature. On the one hand, Devic et al [24,50] presented a method of calculating a net OD and in further consequence introduced a polynomial fitting function, which is also the basis of the calibration curve used in this work, as expressed in section 2. However, the producer Ashland recommends a rational fitting function and to directly allocate the raw values to values in the unit Gray. [23,51] The net OD is a strictly monotonically increasing function of the dose. This and the fact, that the point distribution in figure 3.1 roughly looks like a polynomial of even-numbered degree, justifies the use of a polynomial fitting curve. Furthermore, it can therefore intuitively be assumed, that wave-shaped manifestations, which are a well known problem when fitting polynomially, are negligible.

For the above described reasons, the result should negligibly be influenced, when switching to the fitting process recommended by Ashland. This is important, as the dosimetric method should not influence the overall outcome of this research.

The entire dose evaluation process is based on single channel dosimetry, as only the calibration curve and raw value distributions obtained from the scanner, were considered for the red channel. It was stated elsewhere [54,55], that multichannel dosimetry has a number of advantages over single channel dosimetry, such as allowing for separating the scanned signal into dose dependent and dose independent parts. Furthermore, it is possible to account for nonuniformities in the coating of the film and to correct errors caused by the scanner [54]. This was shown to lead to a higher accuracy of triple channel dosimetry over single channel dosimetry.

As mentioned previously, the latest generation of radiochromic films, EBT3 films were used for the measurement. Although, there are advantages concerning its predecessor in terms of prevention of Newton rings and a symmetrical structure, there was no significant difference found as far as its properties such as dosimetrical behaviour is concerned. [68]

Although single channel dosimetry is a reliable way of dose evaluation, the literature including the manufacturer recommends the introduction of triple

channel dosimetry for the advantages stated above.

4.2 Discussion of the GPR-concept and its presentation in literature

The GPR-concept deserves a further discussion in terms of highlighting its characteristics and dependencies, because it is of major importance in this work.

Although criteria of 2 mm/2% and 3 mm/3% are widely used and accepted in literature, [11–12,21,43,50], more parameters need to be defined to allow for comparison of different studies and publications using the same criterion. For instance, the actual GPR-value highly depends on the grid distance used, as was also shown by Steers et al.[43] If a criterion of 2 mm/2% is chosen, the identical point in the other plan has a deviation of $> 2\,\%$ and the distance between the grid points of both planes is 2 mm, there is only a chance in passing the criterion, if the dose deviation between a point and one of its not diagonal neighbours is exactly zero, which is rather unlikely in clinical practice. Further, if the distance between grid points is decreased, more points are covered by the 2 mm-range and the probability of passing the gamma criterion increases. So far, there is no accepted value for grid distances given in the literature, though there are recommendation of choosing the grid size smaller or equal to one third of the DTA. This is one of the main reasons for the incomparability of the results of different studies and makes the reproducibility barely possible.

Furthermore, the GPR-value depends on the matrix size and on the area irradiated. The bigger the matrix containing a dose distribution of a fixed size is, the more low dose or even no dose areas will be taken into account, which naturally leads to a higher GPR-value, as not irradiated areas are equal. To avoid this effect, in clinical practice, as it is in this work, a threshold of 10% or 20% of the maximum dose is used, under which the dose points are not part of the analysis. However, there is also no accepted parameter in the literature but would be important to guarantee comparability and reproducibility. A more detailed presentation of the parameters leading to the results would be helpful.

It was also shown, that a high GPR-value does not necessarily indicate a correct treatment plan as far as DVH errors are concerned [12] and that different quality assurance (QA) procedures in radiation therapy using the same GPR-criterion can lead to different results in terms of accepting or rejecting a plan. [45] This questions the practicability and benefit of the GPR-analysis and its current usage in clinical practise for QA purposes.

The author strongly suggests the development of a more standardized model and the presentation in literature of all parameters impacting the result to allow for a better comparison of QA procedures. This surely is helpful for every radiation therapy facility, as it is far easier to improve and develop its QA if a direct comparison between the results of other facilities is possible.

4.3 Three-dimensional GPR-analysis using 3D Slicer

Overall, the comparison of clinical with modified beam model shows a rather high passing percentage between 98.5% and 99.98% for prostate boost treatment plans (2), HN (3) and prostate ln (4) plans, as shown in table 3.2. Only the brain metastases show on average a lower GPR, which can be explained with the smaller typical volume of this malignancy. They lead to smaller leaf gaps and in further consequence to a potentially higher error.

When analyzing the three-dimensional gamma map provided by Slicer, interesting anomalies in the regions of steep dose gradients where found. This was investigated by comparing the gamma map with treatment plans in Monaco. Much less points are passing the gamma criterion in regions of higher gradients, than compared to areas of lower dose gradients. Planes showing this phenomenon distinctly, are pictured in figure 4.1 for a HN plan. Here, the coronal, transversal and sagittal gamma map planes are shown. Green corresponds to a GPR close or equal to one, yellow is around one and deep red corresponds to a value of 2, which also represents the maximum gamma value possible for one pixel. The transversal picture, in which the GPR is particularly low corresponds to a plane in the direction of the plane of the drawing of (a) and (c) extracted from the region marked by the black arrows.

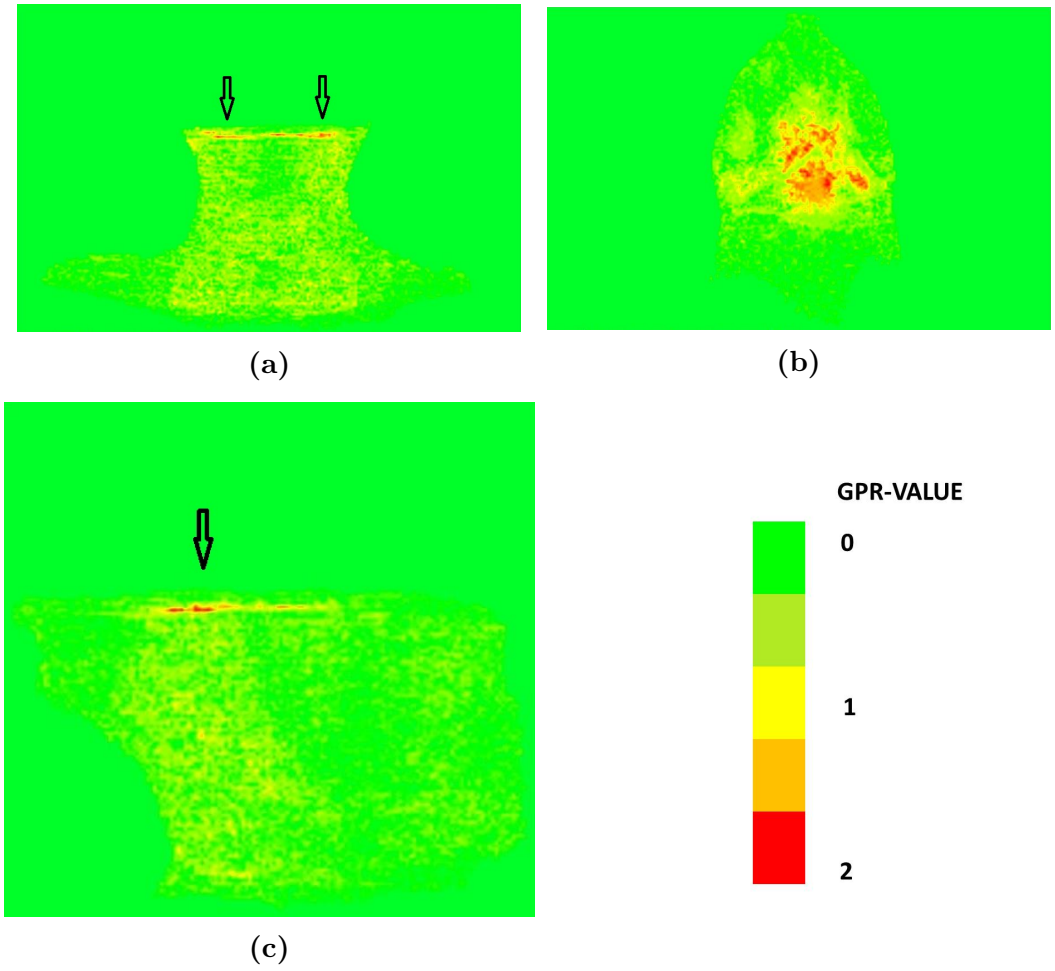

Figure 4.1: Display of a coronal (a), transversal (b) and sagittal (c) plane of the gamma map of a Head & Neck treatment plan using Slicer. The anomaly occuring at steep dose gradients is indicated with black arrows. The overall GPR in this case was 99.29 %.

The effect of higher gamma values at steeper dose gradients was discovered in every plan, but with varying intensity. It was aimed to correlate the markedness of this phenomenon with the overall GPR, by empirically allocating numbers, and conducting a correlation analysis by Spearman, as explained in section 2.5. However, although a value of $\rho_{Spearman} = -0.11$ was calculated, indicating a lower GPR at higher numbers allocated, the p-value was 0.60 and therewith much greater than the widely used criterion of $\alpha = 0.05$ indicating the significance level. So, no significance was found, which probably means, that this effect does not contribute to the overall GPR.

One could assume, that small field errors are the reason why these areas of low GPR occur. If so, the leaf pairs responsible for beam limitation in this area must be closer together than elsewhere. In order to investigate that, the mean aperture length for each leaf pair over an entire treatment plan irradiation procedure was extracted. Although the leaf apertures in this region where indeed small, other areas were observed having mean leaf apertures of similar size, but with higher GPR. Therefore, no correlation between small fields and low GPR in this region could be observed.

4.4 GPR-analysis based on film measurements

Section 2, basically describes an in-house developed procedure to compare calculated planar dose distributions to measured ones based on film dosimetry. Although, every step in this procedure was processed carefully, simply the fact that there are more working steps makes it more error-prone. Firstly, the film scans were made using a scanning correction, which was part of an other in-house project. The concept of dose distribution matching introduced in section 2.4.3, i.e. the self-made MATLAB program for matching of calculated and measured dose distribution is, although conceptionally intuitive and justified, not thoroughly long-term tested. However, developing such procedures and programmes surely has its advantages in terms of higher flexibility concerning different project scopes and probably a better understanding of the chemical and physical phenomenons.

In this context, it should be remarked, that there is a commercialized film manipulation software, namely film QA Pro provided by Ashland. This software

is also capable of calculating GPR. It is questionable, if it is more reasonable in the long run to further develop own programmes or use commercialized software for evaluation. Both approaches surely have advantages. However, it would be interesting, to compare the results obtained in this study with the ones coming from a commercialized software. This is, though, beyond the scope of this study.

The plane matching procedure was made using the measured plane and both the calculated plane based on the clinical BM and the modified BM. In other words, for one measured result, the matching procedure was done twice. So, the coordinates of the planes matched relative to each other at the first matching process should not differ from the second one, as it is the same dose distribution. In most of the cases this was fulfilled well. However, at some plans there was a difference of the relative coordinates of 1 mm noticed, vertically or horizontally, or both. This contributes slightly to the output uncertainty.

As mentioned in section 3.4, significant ($p < 0.05$) differences between GPR based on the clinical BM and the one based on the modified BM were found for the prostate with lymph node treatment group and the head & neck treatment group. In both cases, the GPR based on the modified BM was, in contrast to the expectations, statistically higher. There are however a number of reasons for this phenomenon. Firstly, all potential error sources not only concerning the films and its calibration, but also at all manipulation processes to calculate the GPR must be considered. Secondly, there is a daily variation of the linac output and behaviour itself, which could have led to this result. Although a p-value below a threshold of $\alpha = 0.05$ was considered to be significant, the lowest p-value calculated was 0.035, and therewith not far below this threshold. There is the chance, that the result only appears to be correlated.

A previously conducted study investigating the properties of plans based on the same BM and OFs[21] using a Delta-4 phantom noticed rather high GPR of mostly $> 90\,\%$ for both BM. Also the modified BM was therefore found to be well within limit of clinical acceptance. [21] Basically, the results in this study also follow this trend of high GPR, but it must be remembered, as mentioned in section 2, that for VMAT plans the GPR was up-scaled by increasing the matrix resolution. This is justified, as it was done equally for clinical and modified BM within a treatment group. Therefore the trend, if existing, would

be conserved. However, the IMRT GPR was not up-scaled and shows values mostly over 90 %, except for a couple of outliers which are scarce below this threshold.

It is difficult to estimate quantitatively in what way the above mentioned contributors of error are actually leading to a distortion of the results presented. However, it must be kept in mind when discussing the results.

4.5 Analysis of field sizes and error modelling

It is evident, that when comparing figure 3.3b and 3.4b the distribution's maximum in 3.4b is much lower relative to the maximum at higher aperture lengths than in 3.3b. This occurs because of the fact, that less dose is delivered by smaller fields, when assuming equally distributed irradiation.

As can be seen in table 3.6, all VMAT plans overall show a higher mean error factor than IMRT plans. The latter have, depending on the treatment group, error factors between 1.049 and 1.060, while VMAT factors are between 1.08 and 1.084. When looking at figure 3.2 a trend of small leaf aperture length maxima at this VMAT plan can be seen. This trend is also distinct at all other VMAT plans. An obvious correlation between this trend and the higher mean error factors can therefore be qualitatively stated.

Error Modelling

It must be noted, that the fitting curve in (2.2) has a pole at $x = 0$. This surely can be a problem if the field lengths are extremely small, as the error factor then could have values between 1 and infinity, which is not thought to be reasonable. Furthermore, the entire error factor would be highly dominated by very small lengths and corners, which intuitively cannot be the case. For that reason a threshold was introduced. This limit is set to be 1.18, as it carries forward the basic trend of figure 2.1. This factor is thought to be the error factor corresponding to a 0.5 cm $\times$ 0.5 cm field. Additionally, the threshold occurrence was recorded during evaluation. If the limit is too low, a vast majority of factors for each leaf pair, as introduced in section 2.5, will have exactly this value, resulting in a distortion of the result.

Also, the properties of the fitting procedure itself must be investigated. Due to

the relatively small amount of points for quadratic field error factors, as shown in table 2.1, a fit has a higher uncertainty. Especially at aperture and field sizes smaller than $1\,\text{cm} \times 1\,\text{cm}$, the corresponding fit value can only be seen as an estimation. Therefore the result is dependent on the fit procedure and the chosen curve. It should be remarked in this context, that the computational development of an error model mapping small field uncertainties has never been scientifically tackled before.

Field Size Correlation

The values $\rho_{Spearman}$ and p shown in table 3.7 did not show a significant correlation for any treatment group, neither for iPlan (IMRT) plans nor for Monaco (VMAT) plans. All p-values are higher than 0.1 and Spearman's rho does not indicate a trend, as there are positive and negative values. It can be stated therefore, that the error factors and corresponding GPR are completely uncorrelated.

One of the reasons for the lack of correlation could simply lie in the fact that there is no correlation between GPR and error caused by small fields. However, the manifestation of one or more errors explained above and in section 4.1 and 4.3 could also have led to a significant distortion, resulting in no visible correlation. Finally, there is the uncertainty, that the error model could simply not map the reality properly.

4.6 Additional concept of modelling a MLC in the context of small field errors

The model presented in section 2.5 is only one possible approach out of many potentially promising models systematically mapping the error caused by small fields. Another technique can be derived from Clarkson's integration model. [53] This method was recently applied in carbon ion radiotherapy. [56] A major difference between the originally proposed integration method and the model presented in this chapter is, that no scatter contributions are calculated, but rather different lengths representing the error indicators.

In this model, only considering a single leaf constellation, the length between a point of interest (e.g. the isocenter) and the next beam limiting leaf in one

direction is calculated. This is done for 360 degrees, computing $\frac{2\pi}{\phi}$ different lengths. A graphic outline is shown in figure 4.2. After summing over all lengths and calculating the mean value, this would give a mean length indicating the error at that point. Indeed, to achieve a reliable result, this procedure needs to be done for a larger amount of points equally distributed on a grid within the gaps formed by the leaf arrangement, as indicated by the black points in figure 4.2. Otherwise, one or more points would be favoured.

By averaging, again a mean length can be calculated. Finally, this procedure must be applied to all control points within a treatment plan, leading to an error value for small fields. Also in this model, similar to the one explained in section 2.5., a threshold indicating the maximum error factor would have to be introduced, as points on the imaginary grid could get arbitrarily close to the next leaf, resulting in an overestimated error factor.

This model will probably need considerably more CPU time than the one presented in section 2.5. One reason for this is the angle ϕ, which has to be small to allow for a sufficient accuracy. The length calculation around 360 degree will have to be done at each grid point again demanding considerable CPU time, as the grid should at least have 5 points per leaf, wich would lead to an approximate matrix size of 400×400. Furthermore, a difficulty as far as the computational implementation is concerned, lies in changing from polar coordinates, which denote the rotation, to Cartesian coordinates, which are the basis of the grid containing the leaf and jaw positions.

The actual implementation of this model is, though, beyond the scope of this study.

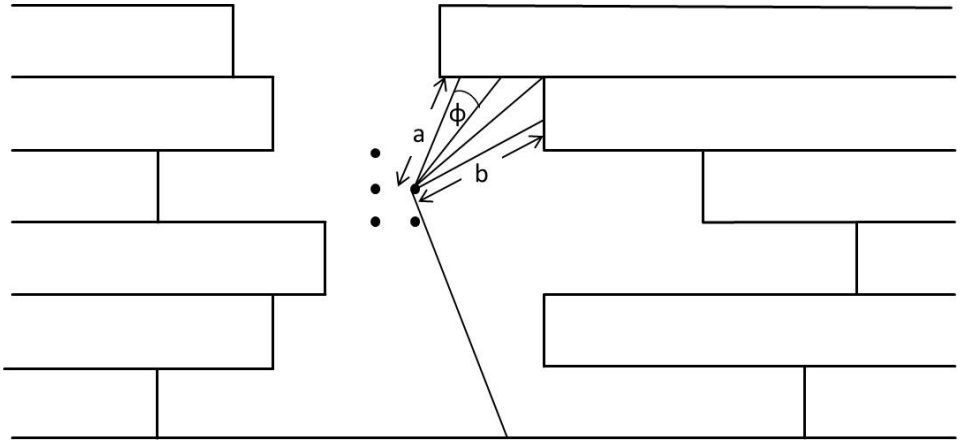

Figure 4.2: The basic concept of small field error modelling based on Clarkson integration[53]. The length between a point of interest and the next beam limiting leaf in one direction is calculated discretely for 360 degree. ϕ is the indicator for the calculated length density.

Chapter 5

Outlook and conclusion

A previously conducted study aiming at detecting small field errors was conducted using a diode array for measurement, the Delta-4 phantom. The resolution of 5 mm × 5 mm motivated the need for a more precise detecting instrument, such as radiochromic films, as used in this study. Furthermore, the systematic mapping of these small field errors was desired, as current literature does not show any research regarding this.

The analysis conducted with 3D Slicer, showed interesting anomalies in areas with steep dose gradients. So far, it was not possible to find a specific reason for this, but it could be used to identify regions sensitive to variations of OFs. Further conducting studies would surely be of interest, eventually resulting in the investigation of quantifiable occurrence of these sensitive areas.

A statistical analysis of the GPR based on a BM with erroneous OFs and the GPR based on a clinically used BM, each of which compared to the actual measurement, showed a significant difference for two treatment groups (Prostate including lymph nodes and Head & Neck) in terms of higher GPR for the BM based on modified OFs. There can be multiple reasons for this occurence and it is difficult to favour a single reason, as discussed above. The main conclusion drawn here, is that the noise and potential errors definitely contribute considerably to the actual results. Another insight of major importance is the fact, that both BM are generally within the range of clinical acceptance i.e. they show a GPR of $> 90\,\%$ for a criterion of $3\,\%/3\,\text{mm}$. The small number of outliers below this threshold are within the uncertainty. Despite focussing

on the 3 %/3 mm criteria, some randomly chosen plans were evaluated with a 2 %/2 mm criteria. The results reflected the basic trend of the outcome based on the 3 %/3 mm criteria. A further analysis would have been beyond the scope of this study.

Overall, in this study there was no correlation found between the computationally self-developed model generating small field error factors and the results of the GPR-analysis comparing measured planar dose distributions with calculated ones. The computationally implemented error model was extensively described in section 2.5 and discussed in section 4. Although it is based on a number of assumptions, it is rather intuitive and could indeed properly indicate the error caused by uncertainties in small field dosimetry. A supportive aspect of the actual magnitude of error factors, was found by comparing the histograms of leaf aperture lengths for IMRT and VMAT with the result, that VMAT show both higher low field occurrences and also higher generated error factors. However, the higher error factors did not show a generally lower GPR at the considered treatment groups for VMAT.

It is considered to be important as part of a scientific approach to devise and develop models trying to match the reality as good as possible, which is the reason why another model based on the integration concept of Clarkson [53,56] was outlined. Although no correlations were found, the measurement methods and the model itself can surely be improved, eventually leading to a lower noise and better error indicator respectively, so that indeed correlations could be found.

It is of great interest, when using radiation therapy applications in clinical treatment procedures to obtain a precise picture of all possible uncertainty influences including the ones caused by small fields. There will surely be a number of other studies conducted, to make state-of-the-art technologies such as IMRT and VMAT even more precise and reliable.

Bibliography

[1] World Cancer Report 2014, World Health Organization (2014)

[2] R. Mohan, C. Chui, L. Lidofsky, "Energy and angular distributions of photons from medical linear accelerators," Medical Physics **12**, 592 (1985)

[3] R. Mohan, C. Chui, L. Lidofsky, "Differential pencil beam dose computation model for photons," Medical Physics **13**, 64 (1986)

[4] R. Mohan, C. Chui, "Use of fast Fourier transforms in calculating dose distributions for irregularly shaped fields for threedimensional treatment planning," Medical Physics **14**, 70 (1987)

[5] Technical Reference Guide, Volume 1/2, Revision 1.8 Brainlab AG, Freiburg, Germany

[6] A. Ahnesjö, "Collapsed cone convolution of radiant energy for photon dose calculation in heterogeneous media," Medical Physics **16**, 577 (1989)

[7] M. Fippel, "Fast Monte Carlo dose calculation for photon beams based on the VMC electron algorithm," Medical Physics **26**, 1466 (1999)

[8] M. Fippel, F. Haryanto, O. Dohm, F. Nüsslin, S. Kriesen, "A virtual photon energy fluence model for Monte Carlo dose calculation," Medical Physics **30**, 301 (2003);

[9] I. Kawrakow, M. Fippel, and K. Friedrich, "3D electron dose calculation using a Voxel based Monte Carlo algorithm (VMC)," Medical Physics **23**, 445 (1996)

[10] W. R. Nelson, H. Hirayama, and D. W. O. Rogers, "The EGS4 Code System," SLAC Report No. SLAC-265 (1985).

[11] D. A. Low, W. B. Harms, S. Mutic, James A. Purdy, "A technique for the quantitative evaluation of dose distributions", Medical Physics **25** (5), 1998

[12] H. Zhen, B. E. Nelms, W. A. Tome, "Moving from gamma passing rates to patient DVH-based QA metrics in pretreatment dose QA, " Med. Phys. 38(10), 54775489 (2011)

[13] D. Georg, T. Knöös, and B. McClean, "Current status and future perspective of flattening filter free photon beams," Medical Physics **38**(3):12801293 (2011).

[14] G. Kragl, F. Baier, S. Lutz, D. Albrich, M. Dalaryd, B. Kroupa, T. Wiezorek, T. Knöös, D. Georg, "Flattening filter free beams in SBRT and IMRT: Dosimetric assessment of peripheral doses, " Medical Physics **21** 91101 (2011)

[15] W. Lechner, H. Palmans, L. Slkner, P. Grochowska, D. Georg, "Detector comparison for small field output factor measurements in flattening filter free photon beams, " Radiotherapy and Oncology **109** 356360 (2013)

[16] J. Cashmore, "The characterization of unflattened photon beams from a 6 MV linear accelerator, Physics in Medicine and Biology **53**, 19331946 (2008).

[17] S. Stathakis, C. Esquivel, A. Gutierrez, C. R. Buckey, and N. Papanikolaou, "Treatment planning and delivery of IMRT using 6 and 18 MV photon beams without flattening filter, " Applied Radiation and Isotopes **67**, 16291637 (2009)

[18] P. L. Petti, M. S. Goodman, J. M. Sisterson, P. J. Biggs, T. A. Gabriel, and R. Mohan, "Sources of electron contamination for the Clinac-35 25-MV photon beam," Medical Physics **10**, 856861 (1983)

[19] w. Lechner, "Dosimetric evaluation of flattening filter free photon beams, " PhD Thesis, Medical University Vienna (2014)

[20] P. Mayles, A. Nahum, J. C. Rosenwald, "Handbook of Radiotherapy Physics: Theory and Practice, " Taylor & Francis Group (2007)

[21] L. Nenoff, "The influence of errors in small field dosimetry on dosimetric accuracy of treatment plans," Medical University Vienna, Master Thesis (2015)

[22] R. Alfonso, P. Andreo, R. Capote, M. S. Huq, W. Kilby, P. Kjäll , T. R. Mackie, H. Palmans, W. Ulrich, and S. Vatnitsky, "A new formalism for reference dosimetry of small and nonstandard fields," Med. Phys. **35** (11):5179 86 (2008).

[23] A. F. Lewis, "Practical Guide to Radiochromic Film EBT2/EBT3,"

[24] S. Devic, J. Seuntjens, E. Sham, E. B. Podgorsak, C. R. Schmidtlein, A. S. Kirov and C. G. Soares, "Precise radiochromic film dosimetry using a flat-bed document scanner, " Medical Physics **32** 7 (2005)

[25] www.statistik.at

[26] http://www.cancer.org/treatment/treatmentsandsideeffects/treatmenttypes/

[27] C. A. Perez, L. W. Brady and E. C. Halperin, "Principles and Practice of Radiation Oncology," Lippincott, Williams & Wilkins (2008)

[28] C. X. Yu, G. Tang, "Intensity-modulated arc therapy: principles, technologies and clinical implementation, " Physics in Medicine and Biology **56** R31R54 (2011)

[29] H. Coutard, "The results and methods of treating cancer by radiation," Annals of Surgery **106**, Nr. 4 (1937)

[30] W. U. Laub, T. Wong, "The volume effect of detectors in the dosimetry of small fields used in IMRT, " Medical Physics **30** 3 (2003)

[31] A. J. D. Scott, A. E. Nahum and J. D. Fenwick, "Using a Monte Carlo model to predict dosimetric properties of small radiotherapy photon fields, " Medical Physics **35**, 4671 (2008)

[32] D. M. Duggan and C. W. Coffey II, "Small photon field dosimetry for stereotactic radiosurgery, " Medical Dosimetry **23**, 3 (1998)

[33] I. J. Das, G. X. Ding and A. Ahnesjö, "Small fields: Nonequilibrium radiation dosimetry, " Medical Physics **35**, 206 (2008)

[34] G. Azangwe, P. Grochowska, D. Georg, J. Izewska, J. Hopfgartner, W. Lechner, C. E. Andersen, A. R. Beierholm, J. Helt-Hansen, H. Mizuno, A. Fukumura, K. Yajima, C. Gouldstone, P. Sharpe, A. Meghzifene and H. Palmans, "Detector to detector corrections: A comprehensive experimental study of detector specific correction factors for beam output measurements for small radiotherapy beams, " Medical Physics **41**, 072103 (2014)

[35] P. Francescon, S. Cora and C. Cavedon, "Total scatter factors of small beams: A multidetector and Monte Carlo study", Medical Physics **35**, 504 (2008)

[36] A. O. Sauer and J. Wilbert, "Measurement of output factors for small photon beams, " Medical Physics **34**, 1983 (2007)

[37] P. H. Charles, G. Cranmer-Sargison, D. I. Thwaites, S. B. Crowe, T. Kairn, R. T. Knight, J. Kenny, C. M. Langton and J. V. Trapp "A practical and theoretical definition of very small field size for radiotherapy output factor measurements, " Medical Physics **41**, 041707 (2014)

[38] A. Gustafsson, B. K. Lind and Anders Brahme, "A generalized pencil beam algorithm for optimization of radiation therapy, " Medical Physics **21**, 343 (1994)

[39] "Agility and Integrity R3.x - Information for Treatment Planning Systems, ", Technical Manual, Document ID: 1504231 01, (2013)

[40] J. Maa, Z. Chang, Z. Wang, Q. J. Wub, J. P. Kirkpatrick and F.-F. Yin, "ExacTrac X-ray 6 degree-of-freedom image-guidance for intracranial non-invasive stereotactic radiotherapy: Comparison with kilo-voltage cone-beam CT, " Radiotherapy and Oncology **93**, 602608 (2009)

[41] J. D. Gagneur and G. A. Ezzell, "An improvement in IMRT QA results and beam matching in linacs using statistical process control," Journal of Applied Clinical Medical Physics **15**,5 (2014)

[42] A. Niroomand-Rad, C. R. Blackwell, B. M. Coursey, K. P. Gall, J. M. Galvin, W. L. McLaughlin, A. S. Meigooni, R. Nath, J. E. Rodgers, C. G.

Soares "Radiochromic Film Dosimetry," AAPM Report No. 63, Medical Physics **25**, 11 (1998)

[43] J. F. Steers, B. A. Fraass, "IMRT QA: Selecting gamma criteria based on error detection sensitivity, " Medical Physics **43**, 4 (2016)

[44] S. F. Kry, A. Molineu, J. R. Kerns, A. M. Faught, J. Y. Huang, K. B. Pulliam, J. Tonigan, P. Alvarez, F. Stingo and David S. Followill, "Institutional Patient-specific IMRT QA Does Not Predict Unacceptable Plan Delivery, " International Journal of Radiation Oncology in Biology and Physics **90**, 5, pp. 1195-1201 (2014)

[45] E. M. McKenzie, P. A. Balter, F. C. Stingo, J. Jones, D. S. Followill, and S. F. Kry, "Toward optimizing patient-specific IMRT QA techniques in the accurate detection of dosimetrically acceptable and unacceptable patient plans, " Medical Physics **41**, 121702 (2014)

[46] C. Spearman, "The proof and measurement of association between two things, " American Journal of Psychology **15** 72-101 (1904)

[47] W. W. Daniel, "Spearman rank correlation coefficient, " Applied Non-parametric Statistics, 2nd edition, PWS-Kent, 358-365

[48] Student, "The Probable Error of Mean, " Biometrica **6**, 1 (1908)

[49] S. Devic, J. Seuntjens, G. Hegyi, E. B. Podgorsak, C. G. Soares, A. S. Kirov, I. Ali, J. F. Williamson, and A. Elizondo, "Dosimetric properties of improved GafChromic films for seven different digitizers, " Medical Physics **31**, 23922401 (2004)

[50] P. Mancosu, P. Navarria, G. Reggiori, L. Cozzi, A. Fogliata, A. Gaudino, F. Lobefalo, L. Paganini, V. Palumbo, B. Sarina, A. Stravato, L. Castagna, S. Tomatis and M. Scorsetti, "In-vivo dosimetry with Gafchromic films for multi-isocentric VMAT irradiation of total marrow lymph-nodes: a feasibility study, " Radiation Oncology **10**, 86 (2015)

[51] EBT3 Specifications, www.ashland.com

[52] H Krieger, "Strahlungsmessung und Dosimetrie." Springer, Wiesbaden (2011)

[53] J. R. Clarkson, "A note on depth dose in fields of irregular shape, " The British Institute of Radiology **14**, 255 (1941)

[54] A. Micke, D. F. Levis and X. Yu, "Multichannel film dosimetry with nonuniformity correction, " Medical Physics **38**, 5 (2011)

[55] Triple Channel Technique Film Dosimetry, www.ashland.com

[56] M. Tajiri, T. Maeda, Y. Koba, Y. Isobe, T. Kuroiwa, S. Fukuda, K. Tanimoto, and K. Shibayama, "Calculation method using Clarkson integration for the physical dose at the center of the spread-out Bragg peak in carbon-ion radiotherapy, " Medical Physics **40**, 071733 (2013)

[57] D. Lewis, A. Micke, "State of the Art Film Dosimetry, ", www.ashland.com

[58] G. Kragl, D. Albrich, D. Georg, "Radiation therapy with unflattened photon beams: Dosimetric accuracy of advanced dose calculation algorithms, " Radiotherapy and Oncology **100**, 3 (2011)

[59] Elekta Versa HD Folder, www.elekta.com

[60] www.brainlab.com

[61] "Absorbed doe determinatino in external beam radiotherpy: an internatinoal code of practice for dosimetry based on standards of absorbed dose to water, " IAEA, TRS-398

[62] CRP E2.40.18: Development of Quality Audits for Advanced Technology in Radiotherapy Dose Delivery - Step 7a

[63] www.slicer.org

[64] A. Fedorov, R. Beichel, J. Kalpahy-Cramer, J. Finet, J. C. Fillion-Robin, S. Pujol, C. Bauer, D. Jennings, F. Fennessy, M. Sonka, J. Buatti, S. R. Aylward, J. V. Miller, S. Pieper, R. Kikinis, "3D Slicer as an Image Computing Plattform for the Quantitative Imaging Network, " Magnetic Resonance Imaging **30** (9) 1323-1341 (2012)

[65] www.iaea.org

[66] www.showme.com

[67] www.uc.edu

[68] R. Dreindl, D. Georg, M. Stock, "Radiochromic film dosimetry: Considerations on precision and accuracy for EBT2 and EBT3 type films, " Z. Med. Phys. **24** 153-163 (2014)

[69] www.dkfz.de, Deutsches Krebsforschungszentrum

List of Figures

List of Tables